Characterization of Beam Vibration

Tianye Yang

A thesis
submitted in partial fulfillment of the
requirements for the degree of

Master of Science in Civil Engineering

University of Washington

2016

Committee:
Richard Wiebe
Paolo M. Calvi
Peter Mackenzie-Helnwein

Program Authorized to Offer Degree:
Civil and Environmental Engineering

University of Washington

Abstract

Characterization of Beam Vibration

Tianye Yang

Chair of the Supervisory Committee:
Assistant Professor Richard Wiebe
Civil and Environmental Engineering

A beam is one of the most fundamental elements in structural engineering, mechanical engineering, and aerospace engineering. Moreover, complex structures like large flexible solar arrays, airplane wings, high-rise buildings, and long-span bridges can be often modeled as beam-like members. Therefore, it is important to study the static and dynamic behavior of this element under various loading conditions.

In the analysis and design of beam or beam-like elements, it is sometimes necessary to determine the eigenparameters (natural frequency, mode shape, and modal damping) of the element under axial force (for example pre-stressed elements). The eigenparameters are also important in the application of nondestructive health monitoring of structural elements as a cost-effective way to detect the existence of damage and its extent. However, most of the research has focused on how cracking affects natural frequencies of the element. Very little research has been done in terms of how natural frequency changes within the yielding and strain hardening region (specifically for steel structures).

In this thesis, the relationship between natural frequency and axial force within the linear elastic region, buckling region, and yielding and strain hardening region is investigated using an analytical model, numerical model, and experiments. The effect of plastic deformation on the natural frequency of beams was investigated. Cyclic loading experiments were conducted to study how re-loading stiffness changes within both the elastic and plastic region. Finally, large amplitude vibration (geometric nonlinearity) was investigated both experimentally and numerically. It is hoped that this thesis will provide a summary of the critical behavior of beams, particularly from the linear versus nonlinear, elastic versus plastic, and static versus dynamic points of view.

TABLE OF CONTENTS

Page

LIST OF FIGURES

Figure Number Page

LIST OF TABLES

Table Number Page

ACKNOWLEDGMENT

First and foremost I would like to express my sincere gratitude to my advisor Professor Richard Wiebe for all of his advice and support through the past two years at University of Washington. His guidance helped me in all the time of research and this thesis. I would also like to thank the other members of my committee, Professor Peter Mackenzie-Helnwein and Professor Paolo Calvi, for the assistance and suggestions they provided on this thesis.

I must also acknowledge Yiming Liu and Bill Kuykendall for their assistance and guidance in the structural material lab and mechanical engineering material lab. I also want to thank Hangyu Kim for his help and support in the lab.

I would not have been able to get through graduate school without the company and support from my friends and fellow students. Ashley Heid and Kristina Tsvetanova, the core crew and the extended members Ryan Ganey and Andrew Winter, with whom I spent uncountable hours with over research work and the good times; Yunjie Zhou and Shen Ren who gave me enormous emotional support; and finally my parents.

Chapter 1

MOTIVATION

A beam is one of the most fundamental elements in structural engineering, mechanical engineering, and aerospace engineering. Moreover, complex structures like large flexible solar arrays, airplane wings, high-rise buildings, and long-span bridge can be often modeled as a beam-like member. Therefore, it is important to study the static and dynamic behavior of this element under various loading conditions.

In the analysis and design of beam or beam-like element, it is sometimes necessary to determine the eigenparameters (natural frequency, mode shape, and model damping) of the element under axial force (for example pre-stressed element). For example both a marine riser or a tendon leg platform have to be maintained in tension to prevent buckling due to self-weight [Bokaian, 1990]. The eigenparameters are also important in the application of nondestructive health monitoring of structural elements as a cost-effective way to detect the existence of damage and its extent. Literature studies have shown a numerous amount of research that successfully identified damage on different structural elements and systems based on changes in natural frequencies, such as beams with various boundary conditions [Kim, 2003; Khiem and Toan, 2014; Yuen, 1985] and cables [Lepidi et al., 2009]. However, most of the research has been focusing on how cracking affect natural frequencies of the element. Very few research has be done in terms of how natural frequency changes within yielding and strain hardening region (specifically steel structures).

In this thesis, the researcher studied the relationship between natural frequency and axial force within linear elastic region, buckling region, and yielding and strain hardening region using analytical model, numerical model and experiments. Related damage detection method based on natural frequency change was also developed. Cyclic loading experiments were conducted to study how re-loading stiffness changes within both elastic and plastic region. Finally, large amplitude vibration (geometric nonlinearity) was investigated experimentally.

Chapter 2

LINEAR BEAM VIBRATION

2.1 Introduction

In this chapter, the dynamic response of a fixed-fixed beam within linear elastic region under both axial load and transverse load is studied. As the most common structural and mechanical element, beams have been well studied in the past. The popular beam theories that are in use today include Euler-Bernoulli beam theory and Timoshenko beam theory. The Euler-Bernoulli beam theory assumes that plane sections remain plane through deflection. In other words, the warping and transverse shear deformation are neglected. These assumptions are valid for slender beams. However, for stocky and composite beams, transverse shear is not negligible. Therefore Timoshenko beam theory was introduced. In Timoshenko beam theory, to simplify the derivation of the equation of motion, the shear strain is assumed to be uniform over a given cross section. Additionally, a shear correction factor is introduced to account for this simplification, and its value depends on the shape of the cross section [Timoshenko, 1921; Malatkar, 2003].

Linear vibration of beams and the effect of constant axial load on natural frequency have been well studied in the past. Usually the approximate solutions such as the Rayleigh-Ritz method, Galerkin's technique or the finite element method are used to analyze beam vibration. However sometimes closed form solutions are developed to save a significant amount of computational cost. For example Bokaian [1988, 1990] developed closed form solution to linear beam vibration taking into consideration axial load and bending stiffness.

Ignoring damping effects, Bokaian [1990] solved the equation of motion of beam vibration under a constant compressive force Q with the assumption that the beam material is linearly elastic and the shear deformation and rotary inertia are negligible, which yields:

$$EI\frac{\partial^4 v}{\partial^4 x} + Q\frac{\partial^2 v}{\partial^2 x} + \mu\ddot{v} = 0, \tag{2.1}$$

where E is Young's modulus, I is the moment of inertia, μ is the linear density, and v is the vertical displacement. Then the solution form of equation 2.1 was assumed as

$$v(x) = c_1 \sinh(Mx/L) + c_2 \cosh(Mx/L) + c_3 \sin(Nx/L) + c_4 \cos(Nx/L), \tag{2.2}$$

in which c_1, c_2, c_3 and c_4 are constant coefficients, and M and N are defined as

$$\begin{aligned} M = L\left\{(Q/2EI) + [(Q/2EI)^2 + (\mu/EI)w^2]^{1/2}\right\}^{1/2} = (U + \sqrt{U^2+\Omega^2})^{1/2}, \\ N = L\left\{-(Q/2EI) + [(Q/2EI)^2 + (\mu/EI)w^2]^{1/2}\right\}^{1/2} = (-U + \sqrt{U^2+\Omega^2})^{1/2}, \end{aligned} \tag{2.3}$$

where $U = QL^2/2EI$ is the dimensionless tension parameter, $\Omega = \omega L^2/\sqrt{EI/\mu}$ is the dimensionless angular natural frequency parameter where ω is the angular natural frequency.

Different boundary conditions are then applied to equation 2.2 to get the final characteristic equation. One example, the clamped-pinned boundary condition is provided. Applying the boundary condition $v(0) = 0$, $\frac{\partial v(0)}{\partial x} = 0$, $v(L) = 0$, and $\frac{\partial^2 v(L)}{\partial^2 x} = 0$ yields:

$$M \cosh M \sin N - N \sinh M \cos N = 0. \tag{2.4}$$

By further algebraic manipulation and simplification, the relationship between normalized tension parameter U and normalized natural frequency parameter Ω is obtained as below

$$\Omega = \sqrt{1 + \gamma U} \quad \textit{where} \quad (\gamma < 1). \tag{2.5}$$

As a conclusion, Bokaian [1990] found that equation 2.5 can be used to describe axial force-frequency relationship of all types of beam vibration and the coefficient γ is solely dependent on the boundary conditions. The same method was applied to the compression regime (with a constant compressive force that is smaller than the buckling force) and the same axial force-frequency relationship was obtained [Bokaian, 1988].

Later on, including the viscous damping and viscoelastic damping terms in the equation of motion, the same linear relationship between axial force and the square of the first natural frequency was obtained by Virgin [1993].

This chapter will outline various methods of linear beam analysis, including ABAQUS, analytical method, and experiments. Three methods were used to investigate the natural frequency of a beam. First, the natural frequency can be obtained by solving the homogeneous solution of the equation of motion (Equation 2.20) (i.e. free vibration). Secondly, one can apply a Fast Fourier Transform on the displacement history of a random point on the beam under an impact transverse force to transfer from time domain to frequency domain. Finally, a frequency sweep was applied to investigate the resonance frequency. Even though this may seem to be redundant for the a linear beam model, it provides solid groundwork for the following chapters for the reason that this method produces a robust picture of the behavior of beam vibration.

2.2 Analytical Model

In this work, an analytical beam vibration model subject to both constant axial load and harmonic transverse load is developed to better understand the beam behavior.

2.2.1 Equation of Motion

The Euler-Bernoulli beam model is applied because the experimental specimen used throughout the research has a dimension of 12 in.×0.5 in.×0.031 in. satisfying the thin beam assumption. Compared to the other two dimensions, a thickness of 0.031 in. is rather small and thus shear deformation can be neglected.

Consider a beam under axial load as shown in Figure 2.1, where L is the beam length, EI is the cross-sectional bending stiffness, A is the cross-sectional area, Q is the applied axial force, μ is the mass density per unit length, which can be calculated as $\mu = \rho A$, where

ρ represents mass density per unit volume, x and y are axis coordinates, u and v are the displacements corresponding to the axis, and θ is the rotation angle.

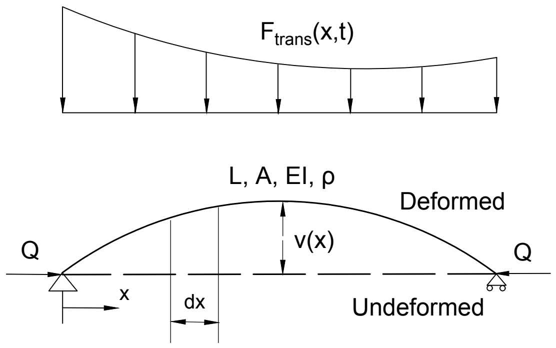

Figure 2.1: Beam under axial load

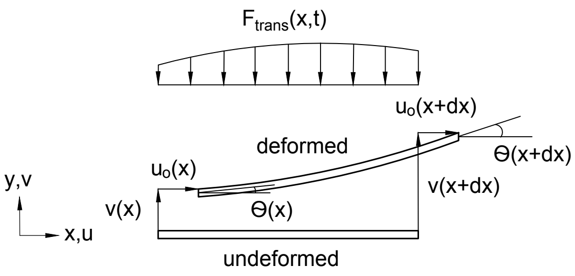

Figure 2.2: A segment of the beam

The free body diagrams of a segment of the beam are as shown in Figure 2.3. The segment of the beam can be analyzed in two different systems. Figure 2.3 (a) shows the free body diagram with axial force, f, shear force, V, and moment, M. Figure 2.3 (b) shows the free body diagram with the ends horizontal force, Q, transverse force, R, and moment, M.

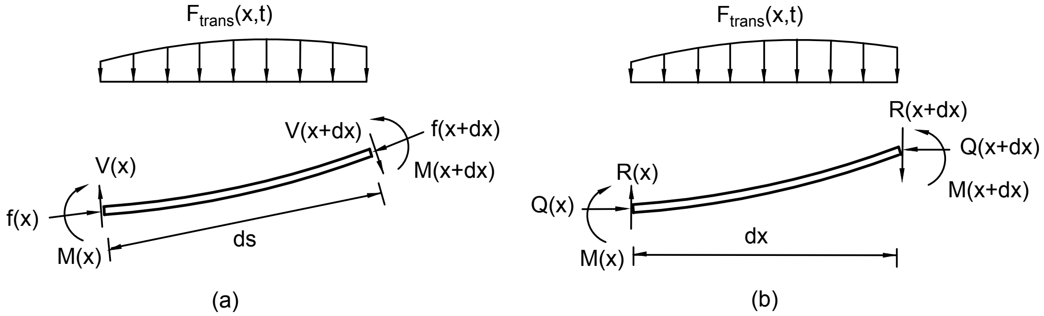

Figure 2.3: Free body diagram of a segment of the beam

The deformed length, ds, can be expressed using:

$$\begin{aligned} ds^2 &= [dx + u_o(x+dx) - u_o(x)]^2 + [v(x+dx) - v(x)]^2 \\ &= dx^2 + (u_o')^2 dx^2 + 2u_o' dx^2 + \mathcal{O}(dx^3) + (v')^2 dx^2 + \mathcal{O}(dx^3) \\ &= \left[1 + 2u_o' + (u_o')^2 + (v')^2\right] dx^2 + \mathcal{O}(dx^3). \end{aligned} \tag{2.6}$$

Ignoring higher order term, one can get

$$ds = dx\sqrt{1 + 2u_o' + (u_o')^2 + (v')^2}. \tag{2.7}$$

Linearizing Equation 2.7, one can obtain

$$ds = dx\left[1 + u_o' + \frac{1}{2}(u_o')^2 + \frac{1}{2}(v')^2\right]. \tag{2.8}$$

Then the axial strain, ϵ, can be expressed as

$$\epsilon = \frac{ds - dx}{dx} = u_o' + \frac{1}{2}(u_o')^2 + \frac{1}{2}(v')^2. \tag{2.9}$$

For some deformation, $u_o' \ll 1$, which leads to $(u_o')^2 \ll u_o'$. However, $(v')^2$ can reach the order of u_o', thus the axial strain expression can be simplified as

$$\epsilon = u_o' + \frac{1}{2}(v')^2. \tag{2.10}$$

Then the axial force, f, can be expressed as $f = -EA\epsilon$. Also, the deformed length, ds, can be shown as $ds = dx(1+\epsilon)$. With small strain and linearization, the following relationship can be obtained:

$$\frac{dx}{ds} = \frac{1}{1+\epsilon} \approx 1 - \epsilon. \tag{2.11}$$

Therefore, $ds \approx dx$.

As is shown in Figure 2.3, using moment equilibrium about the center of the differential element to eliminate shear force, V, one can get

$$\frac{dM}{ds} = V. \tag{2.12}$$

To build the connection between the two free body diagrams, one can get

$$\begin{aligned} \sum F_x: \quad & Q(x) = f(x)\cos\theta(x) - V(x)\sin\theta(x) \\ -\sum F_y: \quad & R(x) = V(x)\cos\theta(x) + f(x)\sin\theta(x). \end{aligned} \tag{2.13}$$

For small rotations, $\theta \ll 1$, one can approximate that $\cos\theta \approx 1$, and $\sin\theta \approx \theta \approx v'$. Then the above equilibrium equations become:

$$\begin{aligned} Q(x) &= f(x) - V(x)v'(x) \\ R(x) &= V(x) + f(x)v'(x). \end{aligned} \tag{2.14}$$

In the scope of this work, shear force is always smaller or approximately equal to axial force, thus $V(x)v'(x) \ll f(x)$. Then one can get $Q(x) \approx f(x)$. However, one can not eliminate the term $f(x)v'(x)$ the same way because $V(x)$ could start as low as zero.

Analyzing the x-direction force equilibrium in Figure 2.3 (b), one can get

$$Q(x+dx) - Q(x) = 0, \tag{2.15}$$

which indicates that $dQ/dx = 0$. Then analyzing the y-direction force equilibrium, one can obtain

$$R(x) - R(x+dx) + F_{trans}(x)dx = 0. \tag{2.16}$$

With $R(x+dx) = R(x) + dR$, the above equation can be further simplified to

$$\frac{dR}{dx} = F_{trans}(x). \tag{2.17}$$

Substituting Equation 2.14 into the above equation, one obtains

$$\begin{gathered}\frac{d}{dx}\left[V(x)+Q(x)v'(x)\right]=F_{trans}(x)\\ \frac{dV(x)}{dx}+\frac{dQ(x)}{dx}v'(x)+Q\frac{d^2v(x)}{dx^2}=F_{trans}(x).\end{gathered} \tag{2.18}$$

Since $dQ/dx = 0$ and $dM/dx \approx dM/ds = V$, the above equation becomes

$$\frac{d^2M(x)}{dx^2}+Q\frac{d^2v(x)}{dx^2}=F_{trans}(x). \tag{2.19}$$

Using linear moment curvature relationship $M = EIv''$ from elastic beam theory and adding inertial force, $\mu\ddot{v}$, and damping force, $\beta\dot{v}$, where β is damping coefficient, one can finally get the equation of motion for linear beam vibration:

$$EI\frac{\partial^4 v}{\partial^4 x}+\mu\ddot{v}+\beta\dot{v}+Q\frac{\partial^2 v}{\partial^2 x}=F_{trans}(x,t). \tag{2.20}$$

Note that damping is the result of energy dissipation during vibration. It is nearly impossible to model damping perfectly but in the scope of mechanical vibrations damping is often considered to be proportional to velocity. The damping coefficient used in analytical and numerical models throughout the research is determined by experiments using the well-known half-power bandwidth method.

2.2.2 Forced Beam Vibration

In order to solve equation 2.20, the harmonic transverse force is separated into a spatial term and a time-varying term. Given by $F_{trans}(x,t) = F(x)\sin\omega t$, where ω represents transverse forcing angular frequency. Applying the assumed particular solution $v_P = A(x)cos\omega t +$

$B(x)sin\omega t$ to the equation of motion yields:

$$\mu(-A(x)\omega^2\cos\omega t - B(x)\omega^2\sin\omega t) + \beta(-A(x)\omega\sin\omega t + B(x)\omega\cos\omega t)$$
$$+ Q(A''(x)\cos\omega t + B''(x)\sin\omega t) + EI(A''''(x)\cos\omega t + B''''(x)\sin\omega t) = F(x)\sin\omega t. \quad (2.21)$$

By using harmonic balance method, the sinusoidal terms can be eliminated as shown below:

$$\begin{aligned} -\mu A(x)\omega^2 + \beta B(x)\omega + QA''(x) + EIA''''(x) &= F(x), \\ -\mu B(x)\omega^2 - \beta A(x)\omega + QB''(x) + EIB''''(x) &= 0. \end{aligned} \quad (2.22)$$

Expressing $A(x)$ in terms of $B(x)$ leads the equation of motion to an 8^{th} order differential equation:

$$\frac{E^2I^2}{\omega}B^{(8)}(x) + \frac{2QEI}{\omega}B^{(6)}(x) + (\frac{Q^2}{\omega} - 2EI\mu\omega)B''''(x) - 2Q\mu\omega B''(x)$$
$$+ (\mu^2\omega^3 + \beta^2\omega)B(x) = \frac{EI}{\omega}F''''(x) + \frac{Q}{\omega}F''(x) - \mu\omega F(x). \quad (2.23)$$

In order to solve the particular solution of equation 2.23, the spatial term of the transverse force is expressed using Fourier Series:

$$F(x) = f_0 + \sum_{n=1}^{\infty}(f_n\cos\frac{2n\pi x}{L} + g_n\sin\frac{2n\pi x}{L}). \quad (2.24)$$

Then solving the constant coefficients ordinary differential equation one can get homogeneous solution $B_H(x)$ and particular solution $B_P(x)$ with an assumed solution form as:

$$B_p(x) = b_0 + \sum_{n=1}^{\infty}(a_n\cos\frac{2n\pi x}{L} + b_n\sin\frac{2n\pi x}{L}). \quad (2.25)$$

Combining with the relationship between $A(x)$ and $B(x)$ obtained from the second equation of Equation 2.22, the particular solution y_P can finally be expressed with known material properties, the Fourier Series coefficients, and 8 unknown constants from solving the 8^{th} order differential equation 2.23. The homogeneous solution y_H is not included in the analytical model because it will decay to zero shortly in the presence of damping. Also, the displacement amplitudes obtained from experiments, which will be discussed later, are all steady-state response. However it should be included if one needs to investigate short-term response, for instance, a beam response under blast loading. In this case, steady-state response is sufficient to indicate the resonance phenomena. By doing a frequency sweep on the analytical model, natural frequency can be found by observing where the resonance occur in amplitude-frequency curve (mid-point maximum displacement amplitude versus forcing frequency). An example is shown in Figure 2.4

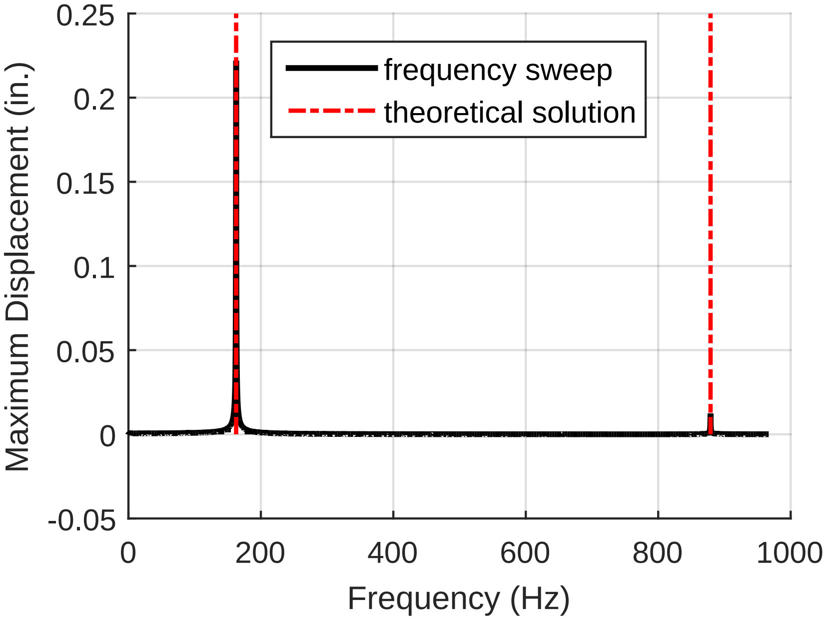

Figure 2.4: Amplitude-frequency curve

As it shown in Figure 2.4, the resonance frequencies obtained from the amplitude-frequency curve matches perfectly with theoretical natural frequency, which can be calculated from the homogeneous part of the equation of motion (Equation 2.20) shown as follows.

$$\mu\ddot{v}_H + \beta\dot{v}_H + QAv''_H + EIv''''_H = 0 \tag{2.26}$$

Using separation of variables assuming $v_H = X(x)T(t)$ one can obtain:

$$\mu X(x)\ddot{T}(t) + \beta X(x)\dot{T}(t) + QX''(x)T(t) + EIX''''(x)T(t) = 0, \tag{2.27}$$

$$\frac{\mu\ddot{T}(t)}{T(t)} + \frac{\beta\dot{T}(t)}{T(t)} = -EI\frac{X''''(x)}{X(x)} - Q\frac{X''(x)}{X(x)} = \lambda. \tag{2.28}$$

From the first part of Equation 2.28, $\ddot{T}(t) + \frac{\beta}{\mu}\dot{T}(t) - \frac{\lambda}{\mu}T(t) = 0$ can be obtained. Then from basic single degree of freedom dynamic vibration equation one can get the relationship between the unknown constant λ and angular natural frequency ω_n as $-\lambda/\mu = \omega_n^2$. Therefore the spatial part can be expressed as

$$-EI\frac{X''''(x)}{X(x)} - Q\frac{X''(x)}{X(x)} = -\mu\omega_n^2. \tag{2.29}$$

With solution form $X(x) = C_1 \sin\Omega_2 x + C_2\cos\Omega_2 x + C_3\sinh\Omega_1 x + C_4\cosh\Omega_1 x$ where C_1, C_2, C_3, and C_4 are constants and

$$\Omega_1 = \sqrt{\frac{-\dfrac{Q}{EI} + \sqrt{\dfrac{Q^2}{E^2I^2} + 4\dfrac{\mu\omega_n^2}{EI}}}{2}}, \qquad \Omega_2 = \sqrt{\frac{\dfrac{Q}{EI} + \sqrt{\dfrac{Q^2}{E^2I^2} + 4\dfrac{\mu\omega_n^2}{EI}}}{2}}. \tag{2.30}$$

Applying the fixed-fixed beam boundary condition $X(x=0) = 0$, $X(x=L) = 0$, $X'(x=0) = 0$, $X'(x=L) = 0$ and algebraic manipulation one can finally get

$$C_1\left[\frac{2\Omega_1\Omega_2 + (\Omega_1^2 - \Omega_2^2)\sin\Omega_2 L\sinh\Omega_1 L - 2\Omega_1\Omega_2\cos\Omega_2 L\cosh\Omega_1 L}{\Omega_2\sin\Omega_2 L + \Omega_1\sinh\Omega_1 L}\right] = 0. \tag{2.31}$$

By solving Equation 2.31, utilizing the relationship between Ω_1 and Ω_2 obtained from Equation 2.30 as $\Omega_2^2 - \Omega_1^2 = Q/EI$, and applying the equation as shown below, theoretical angular natural frequencies can be obtained.

$$\omega_n = \Omega_1 \sqrt{\frac{EI}{\mu}} \sqrt{\Omega_1^2 + \left(\frac{Q}{EI}\right)^2}. \tag{2.32}$$

With this equation developed, one can plot the relationship between f_n^2 and axial force Q since $f_n = \omega_n/(2\pi)$. Below Figure 2.5 shows the f_n^2 versus Q (negative in tension and positive in compression) plot for a 8.25 in.×0.5 in.×0.031 in. steel beam (to match with experiment specimen).

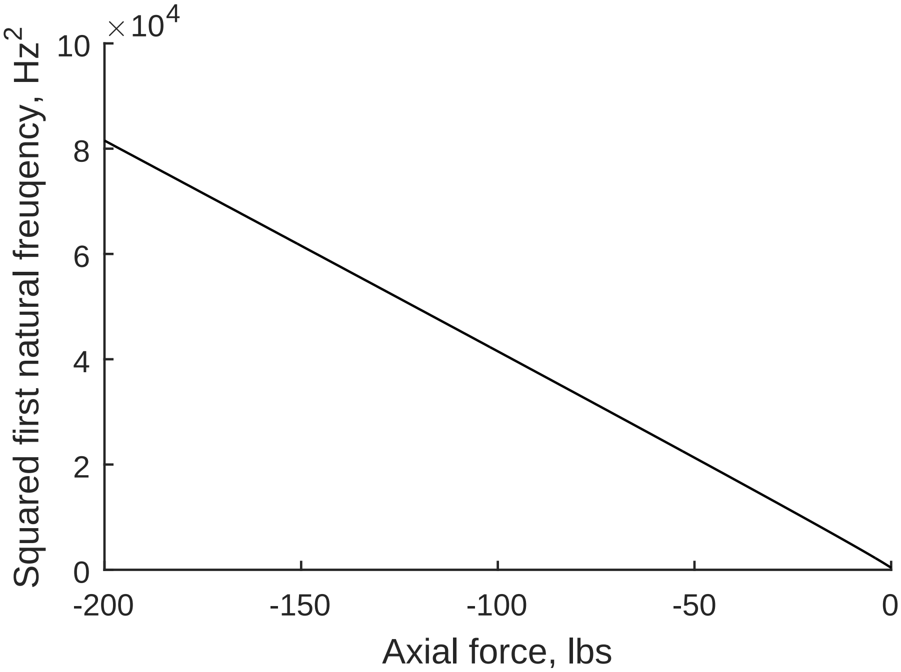

Figure 2.5: Theoretical natural frequency squared f_n^2 versus axial force Q

As it shown in Figure 2.5, f_n^2 and Q has an approximately linear relationship until the compressive force reaches the buckling load (natural frequency reduces to zero), which matches with previous theoretical work.

2.2.3 Free Beam Vibration with Non-Trivial Initial Conditions

Another technique of getting beam natural frequency is to perform an impact test. In order to mimic the impact test in the analytical model, non-trivial initial conditions were applied. With non-trivial initial velocity/displacement, by applying the Fast Fourier Transform to the displacement decay history one can approximate the dominant natural frequencies. A Fast Fourier Transform can convert a signal from its time domain to the frequency domain. It works best when applied to a periodic signal. Therefore an analytical model of free beam vibration with known initial condition is developed in this work. The equation of motion for this case would be the same as Equation 2.26 since no transverse force is applied. However, besides the four boundary conditions, for instance for a fixed-fixed beam $v(x=0) = v(x=L) = v'(x=0) = v'(x=L) = 0$, non-trivial initial conditions $v(t=0) = v(0)$ and $\dot{v}(t=0) = \dot{v}(0)$ are also applied.

Instead of just calculating natural frequencies as in the previous section, the whole beam response needs to be solved in order to perform a Fast Fourier Transform of the displacement history. In the following example, the first five modes are included to achieve a satisfying but not too computationally heavy representation of the beam vibration. Note that the first five modes are sufficient because only a simple sinusoidal initial displacement is applied to the beam. If complicated initial conditions are applied, more mode shapes would be needed to better represent the true beam vibration behavior.

With the first five modes applied, the response can be assumed to be $\sum_{n=1}^{5} T_i(t)X_i(x)$. Continuing the calculation from previous section one can get $X_i(x) = C_i f(x, \Omega_i)$ where

$$f(x,\Omega_i) = [-\frac{\cos\Omega_1 L - \cosh\Omega_1 L}{\sin\Omega_1 L - \sinh\Omega_1 L}]\sin\Omega_1 x + \cos\Omega_1 x + [\frac{\cos\Omega_1 L - \cosh\Omega_1 L}{\sin\Omega_1 L - \sinh\Omega_1 L}]\sinh\Omega_1 L - \cosh\Omega_1 L. \tag{2.33}$$

Solving the time term from separation of variable gives

$$T(t) = e^{-\frac{\beta}{2\mu}t}(c_1\sin\Omega_3 t + c_2\cos\Omega_3 t) \quad \textit{where} \quad \Omega_3 = \frac{1}{2\mu}\sqrt{\beta^2 + 4\mu\lambda}. \tag{2.34}$$

Combining the time and spatial equations using $v = \sum_{n=1}^{5}(T_i(t)X_i(x))$ and applying boundary and initial conditions yield

$$\begin{aligned} C_{1i}f(x,\Omega_i) &= v(0), \\ C_{2i}\Omega_i f(x,\Omega_i) &= \frac{\beta}{2\mu}v(0) + \dot{v}(0). \end{aligned} \tag{2.35}$$

where C_{1i} and C_{2i} are unknown constants that can be solved with a full matrix expansion form using the same idea as Fourier Series. The matrices are as shown below

$$\begin{bmatrix} \int_0^L f_1f_1dx & \int_0^L f_1f_2dx & \int_0^L f_1f_3dx & \int_0^L f_1f_4dx & \int_0^L f_1f_5dx \\ \int_0^L f_2f_1dx & \int_0^L f_2f_2dx & \int_0^L f_2f_3dx & \int_0^L f_2f_4dx & \int_0^L f_2f_5dx \\ \int_0^L f_3f_1dx & \int_0^L f_3f_2dx & \int_0^L f_3f_3dx & \int_0^L f_3f_4dx & \int_0^L f_3f_5dx \\ \int_0^L f_4f_1dx & \int_0^L f_4f_2dx & \int_0^L f_4f_3dx & \int_0^L f_4f_4dx & \int_0^L f_4f_5dx \\ \int_0^L f_5f_1dx & \int_0^L f_5f_2dx & \int_0^L f_5f_3dx & \int_0^L f_5f_4dx & \int_0^L f_5f_5dx \end{bmatrix} \begin{bmatrix} C_{11} \\ C_{12} \\ C_{13} \\ C_{14} \\ C_{15} \end{bmatrix} = \begin{bmatrix} \int_0^L \dot{v}(0)f_1dx \\ \int_0^L \dot{v}(0)f_2dx \\ \int_0^L \dot{v}(0)f_3dx \\ \int_0^L \dot{v}(0)f_4dx \\ \int_0^L \dot{v}(0)f_5dx \end{bmatrix} \tag{2.36}$$

$$\begin{bmatrix} \int_0^L \phi_1\phi_1dx & \int_0^L \phi_1\phi_2dx & \int_0^L \phi_1\phi_3dx & \int_0^L \phi_1\phi_4dx & \int_0^L \phi_1\phi_5dx \\ \int_0^L \phi_2\phi_1dx & \int_0^L \phi_2\phi_2dx & \int_0^L \phi_2\phi_3dx & \int_0^L \phi_2\phi_4dx & \int_0^L \phi_2\phi_5dx \\ \int_0^L \phi_3\phi_1dx & \int_0^L \phi_3\phi_2dx & \int_0^L \phi_3\phi_3dx & \int_0^L \phi_3\phi_4dx & \int_0^L \phi_3\phi_5dx \\ \int_0^L \phi_4\phi_1dx & \int_0^L \phi_4\phi_2dx & \int_0^L \phi_4\phi_3dx & \int_0^L \phi_4\phi_4dx & \int_0^L \phi_4\phi_5dx \\ \int_0^L \phi_5\phi_1dx & \int_0^L \phi_5\phi_2dx & \int_0^L \phi_5\phi_3dx & \int_0^L \phi_5\phi_4dx & \int_0^L \phi_5\phi_5dx \end{bmatrix} \begin{bmatrix} C_{21} \\ C_{22} \\ C_{23} \\ C_{24} \\ C_{25} \end{bmatrix} = \begin{bmatrix} \int_0^L \phi_1(\dot{v}(0) + \frac{\beta}{2\mu}v(0))dx \\ \int_0^L \phi_2(\dot{v}(0) + \frac{\beta}{2\mu}v(0))dx \\ \int_0^L \phi_3(\dot{v}(0) + \frac{\beta}{2\mu}v(0))dx \\ \int_0^L \phi_4(\dot{v}(0) + \frac{\beta}{2\mu}v(0))dx \\ \int_0^L \phi_5(\dot{v}(0) + \frac{\beta}{2\mu}v(0))dx \end{bmatrix} \tag{2.37}$$

where $\phi_i = \Omega_3 f(x,\Omega_i)$

note: $\int_0^L fdx = \sum_{j=1}^{n} f(x_n)$ where n is the total number of nodes of the discretized model.

With C_1 and C_2 solved above, the response of free beam vibration under certain initial conditions can be obtained as follows:

$$v = \sum_{i=1}^{5} e^{-\frac{\beta}{2\mu}t}\sin(\Omega_i t)C_{1i}f(x,\Omega_i) + e^{-\frac{\beta}{2\rho}t}\cos(\Omega_i t)C_{2i}f(x,\Omega_i) \tag{2.38}$$

As mentioned at the beginning of this section, natural frequency of the beam can then be obtained by applying a Fast Fourier Transform to the displacement history of any point on the beam. Note that the disadvantage of this method is that depending on the initial condition, not all dominant natural frequencies (usually only the first three) can be obtained from Fast Fourier Transform. For example, if apply an initial displacement as the exact first mode shape, then only the first natural frequency can be observed from the result plot. Below in Figure 2.6 is an illustration of the result of this method. The model is subject to an initial displacement of a half *sine* wave (i.e. $v(0) = \sin\frac{\pi x}{L}$) and no initial velocity. Below the first plot shows the mid point displacement decaying through damping until it reaches to zero. The second plot is the result of applying a Fast Fourier Transform to the mid-point displacement history. As it can be observed from the plot that even though the displacement history is not periodic, it still matches really well for the first and third natural frequency. However, the second natural frequency is not noticeable in the plot. The reason is that the Fast Fourier Transform is applied to the mid-point displacement history. The second mode happens to have zero displacement in the mid point. Thus the second mode has zero impact on the mid-point displacement. If the quarter-point displacement was chosen, all dominant natural frequencies will be captured.

As a result, in order to capture all the desired natural frequencies, one needs to know the corresponding mode shape well so that nodes of zero displacement or small displacement can be avoided of being chosen.

Another method of obtaining the dominant natural frequency (in this case it is the first natural frequency) from an impact test displacement history is to observe the natural period (time difference between peak to peak from displacement history), then calculate the natural frequency using equation $f_n = 1/T_n$. For example in Figure 2.6, the peak-to-peak time difference can be read as 0.006 *sec.*. Therefore the dominant (first) natural frequency equals approximately to 175 Hz, which matches with both results from Fast Fourier Transform and theoretical model.

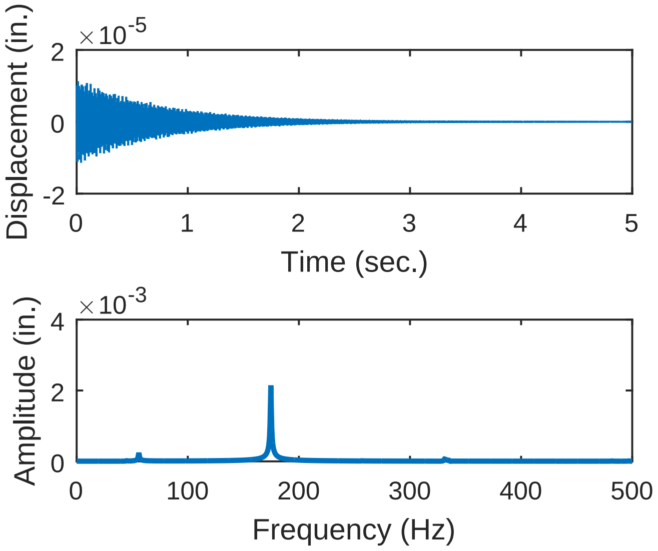

Figure 2.6: Natural frequency from Fast Fourier Transform for a fixed-fixed beam

2.3 *ABAQUS Model*

An ABAQUS beam vibration model is developed to analyze the beam behavior under both transverse and axial loading.

2.3.1 Model Description

Model Properties

For the ABAQUS linear beam vibration model, shell elements were chosen over solid elements for the reason that two dimensions of the specimen are much greater than the third one. When solid elements are used, the bending behavior is usually much stiffer compared with the analytical solution due to the locking phenomenon, especially when the element has one dimension that is much smaller than the other two. To match with the experimental specimen, a shell element with a plane dimension of $8.25in. \times 0.5in.$ and a shell thickness of $0.031in.$ is used for the analysis.

Mass density is taken as $8.8 \times 10^{-3} slugs/in^3$ to match with the analytical model. A bi-linear steel model is used with Young's modulus equal to $20,000ksi$ and a stiffness of $2,000ksi$ after yielding. This bi-linear model is defined for future use in large axial tension analysis, in this chapter the model remains in linear elastic region.

In order to characterize viscous damping in the model, Rayleigh damping is applied, in which the damping is proportional to a linear combination of mass and stiffness as is shown in Equation 2.39.

$$[C] = a_0[M] + a_1[k], \tag{2.39}$$

where [C], [M], and [K] are respectively the damping matrix, mass matrix, and stiffness matrix.

$$a_0 = \zeta \frac{2\omega_i \omega_j}{\omega_i + \omega_j} \quad and \quad a_1 = \zeta \frac{2}{\omega_i + \omega_j} \tag{2.40}$$

Constants a_0 and a_1 are defined as shown in Equation 2.40, where ω_i and ω_j are the angular natural frequencies of two chosen modes i and j with specific damping ratios. Modes i and j should be chosen to ensure reasonable values to represent damping ratios in all the modes that have significant contributions to the response of the specimen. In this model, a point load is applied to the mid-point of the specimen. Thus the first mode is the dominant mode for the dynamic analysis. The first and the fourth mode were chosen to be modes i and j in this case. The damping coefficient ζ of the first mode was calculated as 0.005 from experiments using half-power bandwidth method. The damping coefficient for the fourth mode was assigned as 0.005 as well. Note that with assigned first and fourth modal damping coefficients being 0.005, it can be calculated that the second, the third, and the fifth modal damping coefficient are respectively 0.003, 0.0036, and 0.007. As one can imagine, if the damping coefficients of 0.005 were assigned to mode 1 and mode 2, the higher modes would have comparably high damping coefficients.

With known specimen dimensions, material properties, and a fixed-fixed boundary condition, the first and the fourth theoretical natural frequency of the model can be obtained as 595 rad/sec. and 5290 rad/sec. Then the Rayleigh damping parameters can be calculated using the above equation as $a_0 = 0.85$ and $a_1 = 1.08 \times 10^{-5}$. However, the natural frequencies are relatively insensitive to ζ so more careful analysis was not needed.

Load and Boundary Conditions

In order to study the natural frequency of beam under different axial force, harmonic transverse point load is applied to the center point of the top surface of the beam. The natural frequency can be obtained by varying the frequency of the harmonic transverse force and checking what forcing frequency value causes the resonance phenomenon. The node where the force is applied to is coupled with the horizontal center line of the beam model to avoid in-plane deformation in horizontal direction. A linear elastic material property with Young's modulus equal to $20,000$ ksi was used to avoid local yielding that might be caused from the load, for the reason that local yielding may affect the natural frequency value, which will be illustrated in a later chapter.

The key component of constructing this model is the boundary conditions. In order to achieve a fixed-fixed boundary condition with axial tensile force applied, an additional displacement control step is added to simulate the effect of axial force before applying transverse load. Below in Equation 2.41 is an example of calculating the assigned boundary displacement in the direction of the longest dimension of the specimen (L) to simulate 100 lbf of axial tensile force (displacement and rotation in other directions are constrained to be zero).

$$\Delta L = \epsilon L = \frac{\sigma}{E} L = \frac{Q/d_1 d_2}{E} L = \frac{100/(0.5 \times 0.031)}{20,000,000} \times 8.25 = 0.00266 \; in. \tag{2.41}$$

To avoid sudden change of displacement, i.e. dynamic response, in the analysis, this displacement control step is created to be one second long. The assigned displacement amplitude is reached linearly through this step. A step propagation is used so that the assigned displacement is held to be constant while running transverse force. Figure 2.7 shows a displacement history of the middle point on the fixed end. As desired, a displacement of 0.00266 in. is reached linearly through the first second and then kept constant.

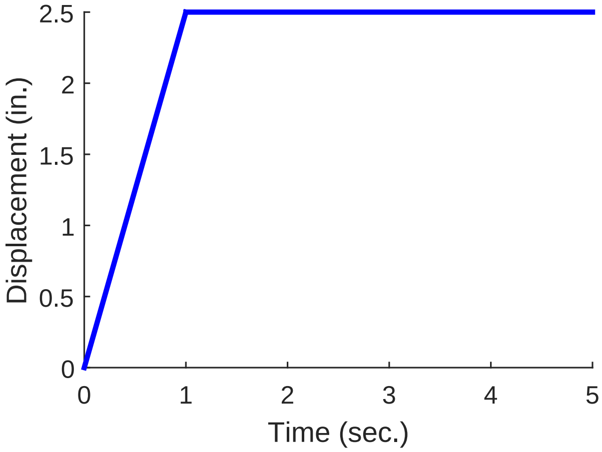

Figure 2.7: Displacement history of the fixed end with assigned displacement

Another way of achieving a similar axial loading and boundary condition is to create a fixed-roller boundary condition that only release one horizontal degree of freedom at one end then apply an axial load on the roller side. However, in this way, with a small axial load, the horizontal displacement of the roller end may varies too much when apply a transverse force, especially when resonance occurs.

Implicit dynamic analysis is used for the analysis. It finds the solution by solving equations involving the current state of the system and the later one. Therefore the solution remains stable no matter what time step is used. Unlike implicit analysis, explicit analysis usually requires very small time steps. However, explicit analysis is much more computationally efficient at a particular time step since there is no matrix inversion involved. In this analysis, because the model is relatively simple, implicit analysis is chosen to ensure stability of the solution.

2.3.2 Results and Analysis

Six models were created by the researcher varying the axial tensile force in order to match with experimental data. The corresponding assigned displacement values can be found in Table. 2.1. For each model, the theoretical first natural frequency was obtained by the analytical model discussed earlier. Then several forcing frequencies starting with a value of $f_n - 10$ Hz. and an increment of 0.1 Hz. were applied to the specimen to obtain what the resonance frequency is. The final results are shown in Table. 2.1 below.

Table 2.1: Natural frequency results from ABAQUS model

Model Number	Tension, lbf	Assigned Boundary Displacement, in	$f_{1theory}$, Hz	$f_{1ABAQUS}$, Hz	$f_{2theory}$, Hz	$f_{2ABAQUS}$, Hz
1	0	0	58.4	60.5	161.2	161.5
2	100	0.00266	205.6	205.3	422.7	423.4
3	200	0.00532	281.4	280.1	570.7	571.4
4	300	0.00798	339.8	339	686.3	686.8
5	400	0.0106	389.3	388.3	784.2	785.4
6	500	0.0133	432.9	432.9	870.9	872.2

As is shown in Table 2.1, the natural frequency values obtained from the Abaqus model match with the analytical results really well.

2.4 Experiments

Experiments are performed to validate the analytical model. This section includes a description of the experimental setup, test procedure, and test results.

2.4.1 Experimental Setup

Figure 2.8: Experimental setup

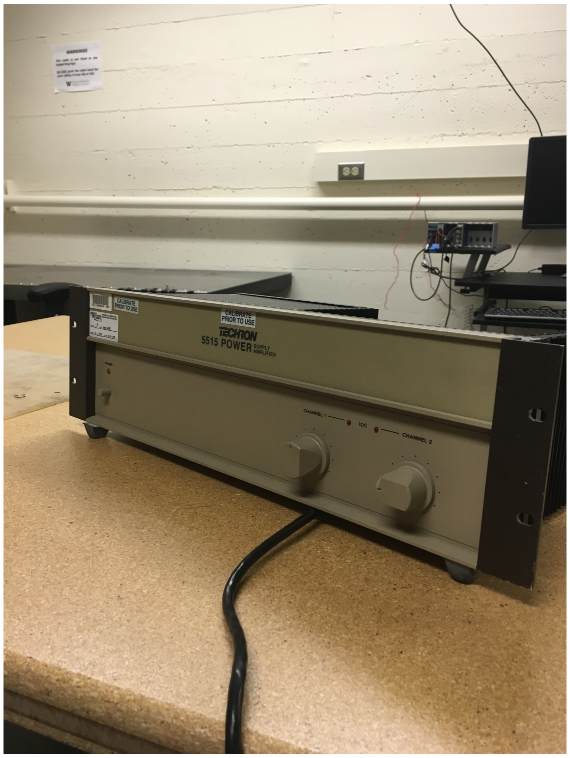

Figure 2.9: Amplifier

As it shown in Figure 2.8, the following are the key components:

Test Specimen

A366/1008 Steel is used throughout the study. A366/1008 steel is generally used for "commercial quality" cold rolled steel. It has comparatively high strength of 50, 000 psi and very good formability. It can generally reach a minimum elongation of 42% to 48%. This material was chosen for the reason that it is able to provide a full picture of how axial force affects natural frequency, especially beyond tensile yield point. Therefore it is preferred that the material demonstrates a clear yielding plateau region and a long strain hardening region so that multiple experimental points can be obtained. The size of the specimen is cut as 12 in.×0.5 in.×0.031 in. One dimension is designed to be significantly smaller than the other two so that transverse shear effect can be minimized and thus the specimen can be better represented by the 2D analytical model.

Loading Device

Instron 5585H is designed to perform material testing. It can be used for tension, compression, bending testing and have a capacity of 56, 250 lbf. As it shown in Figure 2.8, two grips are mounted from the top and the bottom to the machine in order to create a fixed-fixed boundary condition for the test specimen.

Displacement Sensor

Displacement sensor OptoOCDT 2300-20, which can be seen in Figure 2.8 on the right side of the specimen, is used to detect and record the displacement response of any selected point on the specimen. The laser has a sample rate up to 49.2 kHz and an operational range from 50 mm to 60 mm. However, oftentimes a maximum sample rate of 30 kHz is used in order to get bigger measurement range, which is from 40 mm to 60 mm. The resolution of this laser is $0.3 \times 10E^{-6}$ m. It was concerned that there might be troubles detecting any beam deformation during the experiments. Thus a frequency sweep was applied so that the resonance, which causes large vibration amplitude, can be captured by the sensor.

Actuator and Amplifier

A voltage control magnetic force driver is used to simulate a point load on specimen utilizing the magnetic susceptibility of carbon steel. Compared to other actuators, the benefit of using magnetic force driver is that it does not contact the beam so that the beam properties are not affected. Then through Labview, one can control the voltage output (for instance a sinusoid is applied in this experiment) to achieve the desired loading type. With the equation of magnetic force $F = \frac{k}{d^2}$, one can derive the vertical force that is acting on the specimen as follows (horizontal force is neglected and the actuator is treated as a point in this model). Even though this force is very approximate, it is the frequency value that is of primary concern.

$$F(x) = \frac{kd}{[(a-x)^2 + d^2]^{3/2}}, \tag{2.42}$$

where k is an amplitude coefficient, a, d, and x are illustrated as it shown in Figure 2.10. TECHRON 5515 Power Supply Amplifier, as it shown in Figure 2.9, is used to amplify the output voltage amplitude from Labview. The maximum amplification factor this amplifier can achieve is 400. However, it is often found that when it reaches its maximum amplification limit, it tends to distort the force shape (time-varying) from a perfect sinusoidal curve. Thus it is not recommended to perform experiments when the amplifier reaches or is close to reach its limit.

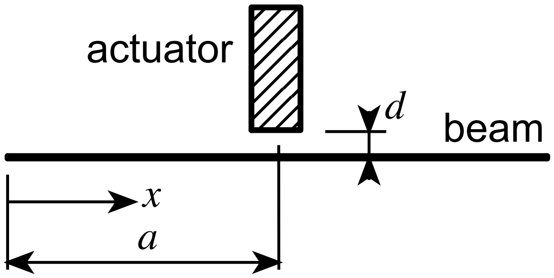

Figure 2.10: Model illustration

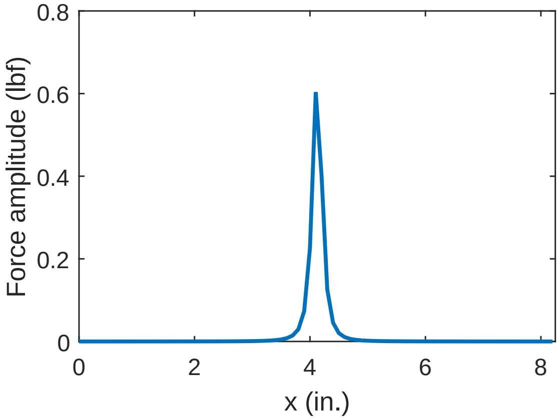

Figure 2.11: Force distribution

2.4.2 Test Procedure

Step 1. Tension Test

Measure dimensions of the specimen after clamp it to the Instron machine (effective length). Perform a tension test so that the researcher can know the approximate yield point and the ultimate strength of the test specimen.

Step 2. Convergence Test

A frequency sweep with an applied voltage output function of $f = \sin{(a + bt)t}$ (where a is initial applied forcing frequency, b is the change rate of applied forcing frequency) is programmed into Labview to output a sinusoidal voltage with a constant frequency sweep rate. In order to capture enough displacement response of each frequency point to obtain a steady-state vibration amplitude, the frequency sweep needs to be slow (i.e. low b value). To achieve a high efficiency as well as satisfying accuracy, a convergence test of what b value needs to be is performed.

Step 3. Obtain the First Natural Frequency for Each Test Point

Force control is used within the elastic region. Based on the stress-strain plot from *Step* 1, 5 points are chosen with a load increment of $1,000$ lbf within the elastic region to perform frequency sweep in order to get the corresponding natural frequency. Due to the limits of the forcing amplitude that the actuator can provide and the resolution of the displacement sensor, higher mode natural frequencies are really difficult to detect with the small displacement response of the specimen under large axial force. Therefore only the first mode natural frequency is studied.

2.4.3 Data Analysis and Results

The stress-strain relationship is obtained from the tension test as it shown in Figure 2.12. As expected, the material presents a clear plateau region and a long strain hardening region before failure. The Young's modulus calculated from the curve is around $20,000$ ksi, which is smaller than what it should be for steel. The potential reason that causes this might be from the slip between the grip and the specimen when the tensile force is applied, which results in a larger strain measurement and thus a smaller Young's modulus. However, this

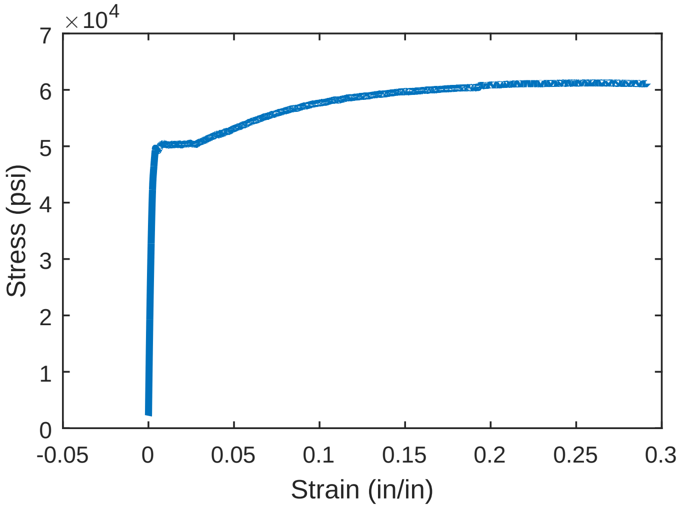

Figure 2.12: *A*366 Specimen stress strain curve

error should not affect the natural frequency results. As will be seen good agreement was obtained in frequency values when modeling using Young's modulus as $20,000$ ksi, which helps verify this result.

Varying the value of b as described in *Step* 2, $b = 0.2$ Hz is chosen to optimize the balance between efficiency and accuracy. Following *Step* 3, a frequency sweep is performed at a varying loading points. Below in Figure 2.13 and Figure 2.14 is one example of how to get natural frequency from the displacement response history under the applied force. par Figure 2.13 shows the mid-point displacement response under a frequency sweep where $a = 100$ Hz and $b = 0.2$ Hz. As can be observed, there is a region in the middle where the displacement amplitude suddenly increases significantly. The resonance happens when the forcing frequency equals the natural frequency. With the a and b values, one can obtain which time period corresponding to a frequency value. Therefore, the mid-point displacement amplitude versus forcing frequency relationship can be obtained as is shown in Figure 2.14. In this case the natural frequency is 117.2 Hz. However, it can be observed that the amplitude-frequency curve is not as symmetric as expected. This phenomenon is caused by the large transverse force amplitude (geometric nonlinearity), which will be discussed in Chapter 6

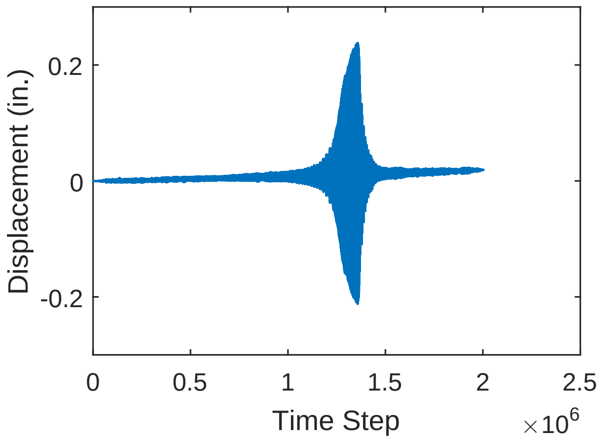

Figure 2.13: Displacement response

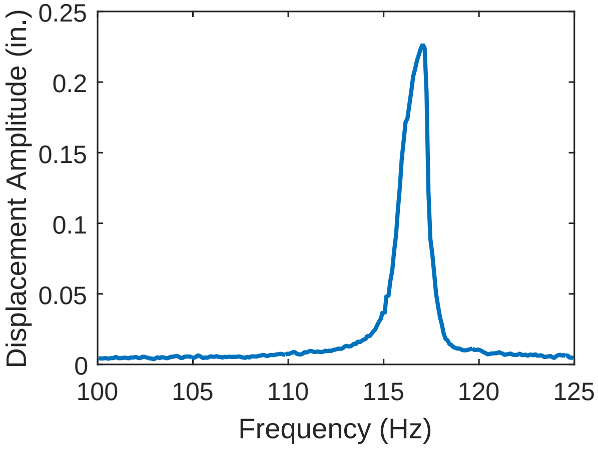

Figure 2.14: Amplitude-frequency curve

in more details. This phenomenon can also be caused by a fast sweep rate. However, convergence test shows that a slower sweep rate yielded the same result.

Two specimens were tested and 5 points were chosen with varying axial force as described in *Step* 3 for each specimen. Applying the same data analysis procedure to each displacement history, Figure 2.15 can be plotted. Comparing with the researcher's analytical model and the previous theoretical work from literature review, the plot shows a similar linear relationship between f_n^2 and Q for both specimen.

As is shown in Figure 2.15, the analytical model and ABAQUS model curves are plotted using the same geometric dimensions as the test specimen. $E = 20,000$ ksi is used to match with the tension test result. A mass density, ρ, value of 8.8×10^{-3} slug/in^3 is used for regular steel since it was not provided by the manufacturer. This was deemed satisfactory as it agrees well with the scale weight. The analytical model shows almost the same curve as the ABAQUS model. The two test specimens show high consistency in the relationship between the squared natural frequency and the axial force. The slight difference between the experimental results and the analytical model may be caused by the inaccurate measurement of the Young's modulus. Nevertheless, all experiments, the analytical model, and the ABAQUS model show a linear relationship between f_n^2 and Q, which matches with the

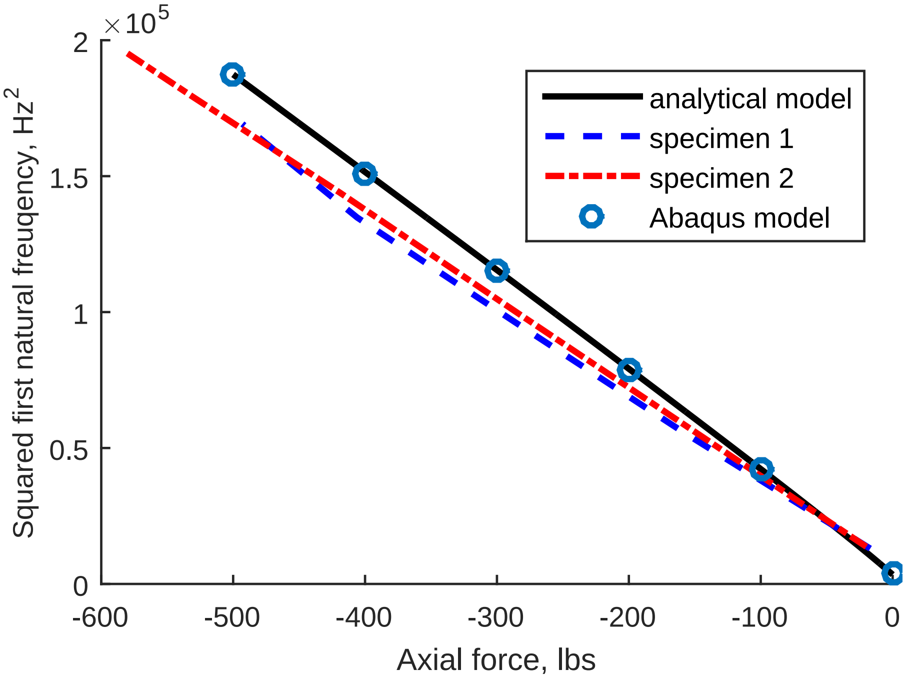

Figure 2.15: Comparison between analytical model, ABAQUS model, and experiments

previous theoretical work conducted by [Bokaian, 1990]

The damping coefficient ζ can also be calculated by using half-power bandwidth method on the amplitude-frequency curve as it shown in Figure 2.16. A natural frequency f_n of 117.2 Hz and resonance amplitude of 0.227 can be observed from the plot. Then one can obtain the corresponding frequency f_a and f_b that have a vibration amplitude as $1/\sqrt{2}$ times the resonance amplitude, which, in this case, $f_a = 116.25$ Hz and $f_b = 117.5$ Hz. Then the damping coefficient ζ can be calculated with Equation 2.43. A derivation of this method can be found in Chopra [2012]. Then the term β in the equation of motion can be calculated using $\beta = 2\zeta\mu\omega_n$.

$$\zeta = \frac{f_b - f_a}{2f_n} \tag{2.43}$$

Five amplitude-frequency curves from the experiment were chosen and an average damp-

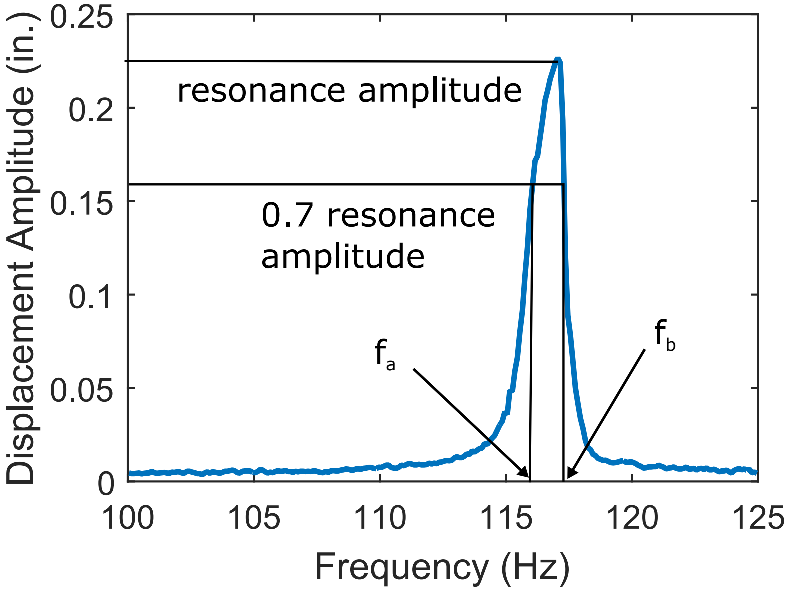

Figure 2.16: Obtaining damping coefficient ζ using half-power bandwidth method

ing coefficient value of 0.005 is obtained for the first mode, which is used throughout this research in all analytical and numerical models.

2.5 Remarks and Conclusion

This chapter includes a thorough study of the effect of axial force on the natural frequency of beam vibration within the elastic region. Even though previous work has been done showing the linear relationship between the square of natural frequency and axial force with varied boundary conditions, a linear beam vibration analytical model as well as an ABAQUS model were developed by the researcher to better understand the full beam response under axial load and any given transverse force. The analytical model and ABAQUS model provide the groundwork for theoretical studies when material nonlinearity is involved in later chapters. Experiments were also conducted to validate the theory. As it shown in Figure 2.15, the plots from experiment results and both analytical and ABAQUS model indicate a high consistency and the results match with previous theoretical work.

Chapter 3

BUCKLING - BEAM VIBRATION UNDER COMPRESSIVE AXIAL FORCE

3.1 *Introduction*

Buckling is one of the most important and most catastrophic failure modes in structural engineering that usually happens to slender element, under large compressive axial force. Theoretically, buckling occurs with a bifurcation in the solution to the equation of static equilibrium. Although it usually causes issues when buckling occurs, a buckled beam can also be used as an isolation device to isolate a mass from it's vibration support [van Ballegooijen, 2010]. Whether it is to be avoided, or exploited, it is important to understand the static and dynamic behavior of buckled beams.

Large amplitude vibration of buckled beams was first investigated by Eisley [1964]. Since then, problems with beams around buckling configurations were studied by many researchers using analytical methods, numerical model, and experiments. An excellent review was done by Ansari et al. [2014]. A numerical solution methodology for analyzing nonlinear forced vibration of postbuckled beams was also proposed in the same article.

What follows in this chapter is a theoretical derivation of calculating the natural frequency of a fixed-fixed beam following the Rayleigh-Ritz method presented in Virgin [2007] and a description of a numerical model of beam vibration with a buckled configuration.

3.2 *Theoretical Derivation*

When nonlinearity is involved, it is easier to solve the problem using energy methods. Based on inextensional beam theory, the total energy stored in a body due to deformation (i.e.

strain energy) can be expressed as:

$$U = \int_0^L \frac{M^2}{2EI} dx = \frac{1}{2} EI \int_0^L v''^{\,2} dx, \tag{3.1}$$

where the prime denotes differentiation with respect to the arc length x. However, the above equation assumes a small deflection by using the linear relationship between moment M and curvature ϕ. If large deflection involved (very likely in buckling configuration), one can use the below equation to express strain energy:

$$U = \frac{1}{2} EI \int_0^L \phi^2 dx, \tag{3.2}$$

where the relationship between curvature ϕ and deflection v for large deflection can be shown as:

$$\phi = \frac{v''}{\sqrt{1 - v'^{\,2}}}. \tag{3.3}$$

It can be shown that this is roughly equivalent to the more well-known Cartesian curvature expression for large curvature (detailed discussion in [Eisley, 1964]). Then the strain energy equation becomes

$$U = \frac{1}{2} EI \int_0^L (v''(1 - v'^{\,2})^{-1/2})^2 dx. \tag{3.4}$$

A Taylor expansion of $(1 - v'^{\,2})^{-1/2}$ about $v' = 0$ is applied to simplify the equation (higher order terms neglected):

$$(1 - v'^{\,2})^{-1/2} = 1 + \frac{1}{2} v'^{\,2}. \tag{3.5}$$

Then the strain energy becomes

$$U = \frac{1}{2} EI \int_0^L (v''^{\,2} + v''^{\,2} v'^{\,2} + \frac{1}{4} v''^{\,2} v'^{\,4}) dx \approx \frac{1}{2} (EI \int_0^L v''^{\,2} + v''^{\,2} v'^{\,2}) dx. \tag{3.6}$$

Another contribution to the total energy is the potential energy V_p from the axial load with an expression of $V_p = P\delta$ where δ is the end shortening in the transverse deflection:

$$\delta = L - \int_0^L \sqrt{1 - v'^{\,2}}dx. \tag{3.7}$$

Again, applying Taylor expansion to $\sqrt{1 - v'^{\,2}}$ about $v' = 0$ one can get

$$\delta = L - \int_0^L (1 - \frac{1}{2}v'^{\,2} + \frac{3}{8}v'^{\,4})dx = \int_0^L (-\frac{1}{2}v'^{\,2} + \frac{3}{8}v'^{\,4})dx. \tag{3.8}$$

Then one can get the expression of the potential energy of the load

$$V_p = P\delta = -\frac{1}{2}P\int_0^L (v'^{\,2} + \frac{1}{4}v'^{\,4})dx. \tag{3.9}$$

For a fixed-fixed beam, assuming Δ is the maximum mid-point displacement history, solution form for buckled shape is assumed as

$$v = \Delta(t)(1 - cos\frac{2\pi x}{L}), \tag{3.10}$$

which fits the boundary conditions $v(x = 0) = v(x = L) = v'(x = 0) = v'(x = L) = 0$. Applying the solution form to the total energy equation $V = U + V_p$, one can obtain

$$\begin{aligned} V(\Delta) &= \frac{1}{2}(EI\int_0^L v''^{\,2} + v''^{\,2}v'^{\,2})dx - \frac{1}{2}P\int_0^L (v'^{\,2} + \frac{1}{4}v'^{\,4})dx \\ &= \frac{1}{2}EI\int_0^L \left[\Delta^2(\frac{2\pi}{L})^2\cos(\frac{2\pi x}{L}) + \Delta^2(\frac{2\pi}{L})^2\cos(\frac{2\pi x}{L})\Delta^2(\frac{2\pi}{L})^2\sin^2(\frac{2\pi x}{L})\right]dx \\ &\quad - \frac{1}{2}P\int_0^L \left[\Delta^2(\frac{2\pi}{L})^2\sin^2(\frac{2\pi x}{L}) + \frac{1}{4}\Delta^4(\frac{2\pi}{L})^4\sin^4(\frac{2\pi x}{L})\right]dx \\ &= \frac{1}{2}EI\left[\Delta^2(\frac{2\pi}{L})^4(\frac{L}{2}) + \Delta^4(\frac{2\pi}{L})^6(\frac{L}{8})\right] - \frac{1}{2}P\left[\Delta^2(\frac{2\pi}{L})^2(\frac{L}{2}) + \frac{1}{4}\Delta^4(\frac{2\pi}{L})^4(\frac{3L}{8})\right]. \end{aligned} \tag{3.11}$$

Taking the derivative of the total energy with respect to deflection, one can get the total force of the system. Setting the total force equal to zero, the equilibrium equation below can be obtained:

$$\begin{aligned}\frac{dV}{d\Delta} &= EI\left(\frac{2\pi}{L}\right)^4\left(\frac{L}{2}\right)\Delta + 2EI\Delta^3\left(\frac{2\pi}{L}\right)^6\left(\frac{L}{8}\right) - P\Delta\left(\frac{2\pi}{L}\right)^2\left(\frac{L}{2}\right) - 2P\Delta^3\left(\frac{2\pi}{L}\right)^4\left(\frac{3L}{32}\right)\\ &= \Delta\left[1 + \frac{1}{2}\Delta^2\left(\frac{2\pi}{L}\right)^2 - \frac{P}{EI(2\pi/L)^2} - \frac{3}{8}\frac{P}{EI}\Delta^2\right]\\ &= 1 + \frac{1}{2}\left(\frac{2\pi}{L}\right)^2\Delta^2 - \Lambda\left(1 + \frac{3}{8}\left(\frac{2\pi}{L}\right)^2\Delta^2\right) = 0,\end{aligned} \tag{3.12}$$

where $\Lambda = \frac{P}{EI(2\pi/L)^2}$ as normalization of the compressive force P. Then the relationship between axial force P and mid-point displacement Δ can be derived

$$\Lambda = \frac{1 + \frac{1}{2}\left(\frac{2\pi}{L}\right)^2\Delta^2}{1 + \frac{3}{8}\left(\frac{2\pi}{L}\right)^2\Delta^2}. \tag{3.13}$$

Applying Taylor expansion and ignoring higher order terms, the above equation becomes:

$$\Lambda \approx 1 + \frac{1}{8}\left(\frac{2\pi}{L}\right)^2\Delta^2. \tag{3.14}$$

In order to get the natural frequency of the buckled beam, kinematic energy T needs to be considered to formulate the dynamic equation of motion.

$$T = \frac{1}{2}m\int_0^L \dot{y}^2 dx = \frac{1}{2}m\int_0^L \dot{\Delta}^2\sin^2(\frac{2\pi x}{L})dx = \frac{1}{2}m\left(\frac{L}{2}\right)\dot{\Delta}^2 \tag{3.15}$$

Then the equation of motion can be formulated as

$$\frac{d}{dt}\left(\frac{\partial T}{\partial \Delta}\right) + \frac{\partial V}{\partial \Delta} = 0. \tag{3.16}$$

Substituting Equation 3.11 and Equation 3.15 in the equation of motion, one can obtain

$$\begin{aligned} \frac{mL}{2}\ddot{\Delta} + EI\left(\frac{2\pi}{L}\right)^4\left(\frac{L}{2}\right)\Delta + \frac{1}{2}EI\left(\frac{2\pi}{L}\right)^6\left(\frac{L}{2}\right)\Delta^3 \\ -P\Delta\left(\frac{2\pi}{L}\right)^2\left(\frac{L}{2}\right) - \frac{3}{8}P\Delta^3\left(\frac{2\pi}{L}\right)^4\left(\frac{L}{2}\right) = 0. \end{aligned} \tag{3.17}$$

For the dynamic response Δ, let $\Delta = \Delta^e + u$ where Δ^e is the mid-point displacement of the equivalent static buckled shape and u is the small vibration response one can use to get the natural frequency about a deformed configuration. With $\Delta = \Delta^e + u$, the following expressions can be calculated

$$\ddot{\Delta} = \ddot{u} \quad and \quad \Delta^3 = \Delta^{e\ 3} + 3\Delta^{e\ 2}u + 3\Delta^e u^2 + u^3 \approx \Delta^{e\ 3} + 3\Delta^{e\ 2}u. \tag{3.18}$$

Then the dynamic equation of motion becomes

$$\begin{aligned} \frac{m}{EI\left(\frac{2\pi}{L}\right)^4}\ddot{u} + \left[1 + \frac{3}{2}\left(\frac{2\pi}{L}\right)^2\Delta^{e\ 2} - \Lambda - \frac{9}{8}\left(\frac{2\pi}{L}\right)^2\Lambda\Delta^{e\ 2}\right]u \\ + \left[\Delta^e + \frac{1}{2}\left(\frac{2\pi}{L}\right)^2\Delta^{e\ 3} - \Lambda\Delta^e - \frac{3}{8}\left(\frac{2\pi}{L}\right)^2\Lambda\Delta^{e\ 3}\right] = 0. \end{aligned} \tag{3.19}$$

From the dynamic equation of motion, the natural frequency ω_n can be expressed as

$$\omega_n^2 = \frac{1 + \frac{3}{2}\left(\frac{2\pi}{L}\right)^2\Delta^{e\ 2} - \Lambda\left(1 + \frac{9}{8}\left(\frac{2\pi}{L}\right)^2\Delta^{e\ 2}\right)}{m/\left[EI\left(\frac{2\pi}{L}\right)^4\right]}. \tag{3.20}$$

With normalization of natural frequency, one can get

$$\Omega^2 = \frac{\omega^2}{EI\left(\frac{2\pi}{L}\right)^4/m}, \tag{3.21}$$

$$\Omega^2 = 1 - \Lambda + \frac{3\pi^2}{2}\left(\frac{\Delta^e}{L}\right)^2. \tag{3.22}$$

Substituting Equation 3.14 in the above equation, the final relationship between natural frequency and axial compressive force (passed buckling load) can be obtained

$$\Omega^2 = 2(\Lambda - 1). \tag{3.23}$$

A similar procedure is applied on a simply supported beam which can be found in Virgin [2007]. The same relationship of $\Omega^2 = 2(\Lambda - 1)$ is found. Therefore it can be concluded that for both simply support and fixed-fixed beam, the linear relationship between the square of natural frequency and axial force remains linear after the buckling force is reached. However, the slope of the plot is doubled after buckling point as compared to the the relationship between the natural frequency and axial compressive force before buckling as derived in Chapter 2.

3.3 Numerical Model

In order to be able to model beam with large displacement, a finite element model with co-rotational beam element was developed as described in Section 3.3.1. The continuum beam is discretized into a finite number of elements and nodes. For each node, the static force equilibrium is applied

$$F^{int} = \lambda F^{ext}, \tag{3.24}$$

where the external force is expressed as a amplitude parameter λ, and a constant shape vector F^{ext}. This nonlinear equation is solved using the arc-length method which will be explained in Section 3.3.2 with $F(\Delta, \lambda) = F^{int}(\Delta) - \lambda F^{ext}$ (where Δ is the mid-point displacement). In order to get the natural frequency of beam under buckling configuration, the same equation as in theoretical model $\Delta = \Delta^e + u$ is applied to the equilibrium equation. Then one can get $F^{int}(\Delta^e + u) = F^{int}(\Delta^e) + Ku$, where $K = \nabla(F^{int})$. Applying this with an assumed solution form $u = \phi \sin(\omega t)$ to the dynamic equation of motion as shown below, one can get

Equation 3.26 (ignoring damping):

$$M\ddot{\Delta} + C\dot{\Delta} + F^{int} = F^{ext}, \tag{3.25}$$

$$\omega^2 M\phi + K\phi = 0. \tag{3.26}$$

The eigenvalues of Equation 3.26 are the natural angular frequencies of the system. If solving Equation 3.25, the dynamic response can be obtained. In this research, Newmark-Beta time integration method is applied as described in Section 3.3.3.

3.3.1 Co-Rotational Beam Element Formulation

This section presents a formulation of a finite element analysis using co-rotational beam element. This derivation closely follows the procedure given by [Wiebe, 2012] . Using this approach a beam is allowed to have large global displacement and rotations as long as small local element strains, which makes the method well-suited for a buckling beam configuration.

This method aims to separate right body motions from strain induced deformations at a local element level so that only the angles of rotation and nodal displacement for a local element are needed in order to solve the unknown degrees of freedom. A tangent stiffness matrix is required for arc-length solutions of this formulation. The derivation of the formulation of this analysis is described as follows.

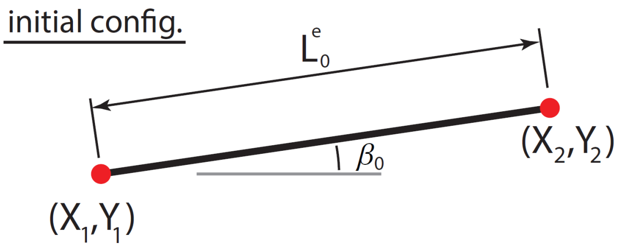

Figure 3.1: Co-rotational finite beam element method [Wiebe, 2012]

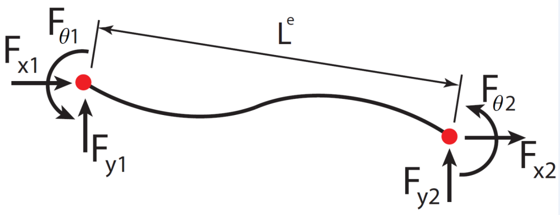

Figure 3.2: Forces in global coordination

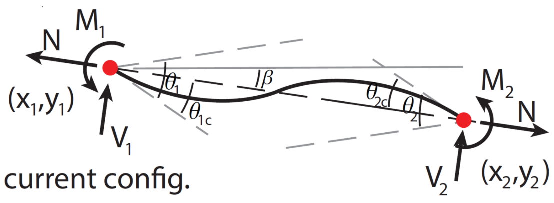

Figure 3.3: Forces in local coordination

As it is illustrated from Figure 3.1 to Figure 3.3, the displacement angle β may be large, the local rotations θ_{1c} and θ_{2c} are small. This method assumes elements remain linear elastic and are initially straight between nodes before loading. As it shown in Figure 3.4, the relationship between the global internal force vector F_e^{int} and local internal degrees of freedom vector (M_1, M_2, N) can be obtained by the force and moment equilibrium as shown below (where the axial force N is assumed to act along the line projected between the end points of the current configuration of the element and the magnitude is only dependent on the length change of this projection):

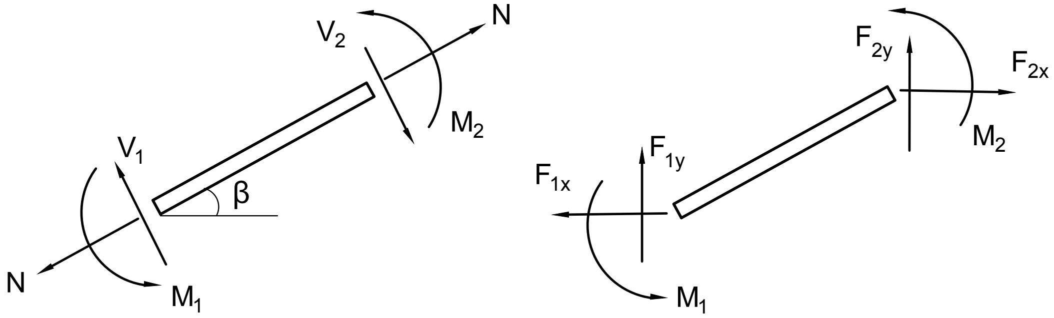

Figure 3.4: Free body diagram with different coordinates

$$\begin{aligned} F_{1x} &= -N\cos\beta - V_1\sin\beta, \\ F_{1y} &= V_1\cos\beta - N\sin\beta, \\ \sum M_2 &= M_1 + M_2 - V_1 L^e. \end{aligned} \tag{3.27}$$

Substituting the moment equilibrium equation into force equilibrium equations, one can get

$$
\begin{aligned}
F_{1x} &= -N\cos\beta - \left(\frac{M_1+M_2}{L^e}\right)\sin\beta,\\
F_{1y} &= -N\sin\beta + \left(\frac{M_1+M_2}{L^e}\right)\cos\beta,\\
M_1 &= M_1.
\end{aligned}
\tag{3.28}
$$

Applying some calculation to the other node 2, one can get the final equation

$$
\begin{gathered}
F_e^{int} = \{F_{x1}\ F_{y1}\ M_1\ F_{x2}\ F_{y2}\ M_2\}^T = B^T\{N\ M_1\ M_2\}^T\\
B = \frac{1}{L^e}, \begin{bmatrix} -cL^e & -sL^e & 0 & cL^e & sL^e & 0\\ -s & c & L^e & s & c & 0\\ -s & c & 0 & s & -c & L^e \end{bmatrix}\\
where \qquad c = \cos\beta \qquad s = \sin\beta.
\end{gathered}
\tag{3.29}
$$

With Euler-Bernoulli beam theory and previous assumptions, the axial force, N, and the moments, M_1 and M_2, can be expressing using local element rotations as follows (assuming small rotations)

$$
\begin{gathered}
N = \frac{EA}{L}(L^e - L_0^e),\\
\begin{bmatrix} M1\\ M2 \end{bmatrix} = \frac{2EI}{L_0^e}\begin{bmatrix} 2 & 1\\ 1 & 2 \end{bmatrix}\begin{bmatrix} \theta_{1c}\\ \theta_{2c} \end{bmatrix}.
\end{gathered}
\tag{3.30}
$$

Based on Figure 3.1, the following relationship can be observed

$$
\begin{aligned}
L_0^{e2} &= (X_2 - X_1)^2 + (Y_2 - Y_1)^2,\\
L^{e2} &= (x_2 - x_1)^2 + (y_2 - y_1)^2,\\
where \quad \theta_{1c} &= \theta_1 + \beta_0 - \beta, \quad \theta_{2c} = \theta_1 + \beta_0 - \beta.
\end{aligned}
\tag{3.31}
$$

With the above equations,the states of the system (x_1, y_1), (x_2, y_2), and (θ_1, θ_2) can be solved. Even though shear force is not calculated in the above equation, it can be easily calculated based on force equilibrium and moment equilibrium listed below

$$\begin{aligned} &V_1 + V_2 = 0, \\ &V_1 = \frac{M_1 + M_2}{L^e}. \end{aligned} \tag{3.32}$$

As mentioned earlier in the section, a tangent stiffness matrix $K = \nabla F^{int}$ is needed for the arc-length method used in the static analysis and the Newmark-beta method used in dynamic analysis, which is given by [Kantz and Schreiber, 1997].

$$\begin{gathered} K_e = B^T D B + \frac{N}{L^e} z z^T + \frac{M_1 + M_2}{L^{e2}} (r z^T + z r^T), \\ where \quad D = \frac{EI}{L_0^e} \begin{bmatrix} A/I & 0 & 0 \\ 0 & 4 & 2 \\ 0 & 2 & 4 \end{bmatrix}, \\ z = \{s \ -c \ 0 \ -s \ c \ 0\}^T, \quad r = \{-c \ -s \ 0 \ c \ s \ 0\}^T. \end{gathered} \tag{3.33}$$

One can use the elemental expressions to assemble the global internal force vector, F^{int}, and the tangent stiffness matrix, K. These two expressions allow one to analyze the static response of beam under buckling configuration. In order to obtain the natural frequency of a buckling beam, dynamic response needs to be investigated, which requires the mass matrix of the system. A lumped mass matrix was found to be more than sufficient to accurately model the inertia force of the system when comparing the natural frequencies obtained numerically with experimental results [Wiebe, 2012]. The lumped mass matrix for a local element is shown below

$$M_e = \frac{1}{2} \rho A L_0^e \cdot Diag \begin{bmatrix} 1 & 1 & L_0^{e2}/12 & 1 & 1 & L_0^{e2}/12 \end{bmatrix}. \tag{3.34}$$

With knowing stiffness matrix and mass matrix, natural frequencies can be easily obtained by solving the eigenvalue problem of Equation 3.26.

3.3.2 Arc-Length Method

Nonlinear system of equations are usually involved in numerical studies. Several techniques has been developed to trace the equilibrium path over the past decades. Load-controlled methods, for instance Euler method (1^{st} order Runge-Kutta method) and Newton-Raphson method, were first invented to solve such problems. However, load-controlled methods are not able to capture equilibrium paths that have a changing slope sign (i.e. limit points). Displacement-controlled methods were then introduced to overcome this issue. Different techniques are used depending on the nature of the problem. Arc-length method was developed as a general method of solving nonlinear system of equations. Arc-length method varies the ratio between load increment and displacement increment (a fixed value of arc-length) until convergence. Below is a general algorithm of arc-length method, which closely follows the procedure described by [Wiebe, 2012].

Considering a nonlinear system of equations that can be represented by

$$F(\Delta, \lambda) = 0, \tag{3.35}$$

where F is a function of the unknown Δ (usually displacement) and a parameter λ, which usually represents load parameter. Using superscript to represent time step and subscript to represent iterations with each time step, the general Taylor expansion of $F(\Delta^i_{n+1}, \lambda^i_{n+1})$ is shown as

$$\begin{aligned} F(\Delta^i_{n+1}, \lambda^i_{n+1}) &= F(\Delta^i_n + d\Delta, \lambda^i_n + d\lambda) \\ &\approx F(\Delta^i_n, \lambda^i_n) + K(\Delta^i_n, \lambda^i_n) d\Delta + F^e(\Delta^i_n, \lambda^i_n) d\lambda. \end{aligned} \tag{3.36}$$

Since the system of equations $F = 0$ (for static beam buckling $F = F^{int} - \lambda F^{ext}$ as described earlier this chapter), the above equation becomes

$$\begin{gathered} K(\Delta_n^i, \lambda_n^i)d\Delta + F^e(\Delta_n^i, \lambda_n^i)d\lambda = -F(\Delta_n^i, \lambda_n^i), \\ \text{where} \quad K = \frac{\partial F}{\partial \Delta} \quad \text{and} \quad F^e = \frac{\partial F}{\partial \lambda}. \end{gathered} \tag{3.37}$$

With the additional unknown $d\lambda$, another restraint for solving the system equation in each time step is the constant value arc-length δa is needed, which is defined below as Crisfield [1981]

$$\begin{gathered} f(\delta\Delta_{n+1}, \delta\lambda_{n+1}) = \sqrt{c(\delta\Delta_{n+1})^T A \delta\Delta_{n+1} + b\delta_{n+1}^2} = \delta a, \\ \text{where} \quad \delta\Delta_{n+1} = \Delta_{n+1}^i - \Delta^{i-1} = \delta\Delta_n + d\Delta, \\ \delta\lambda_{n+1} = \lambda_{n+1}^i - \lambda^{i-1} = \delta\lambda_n + d\lambda. \end{gathered} \tag{3.38}$$

Compared to other nonlinear system of equations solving techniques, one advantage of using arc-length method is that one can control the weight of the load step, displacement step, and the total arc-length by changing the parameters b, c, and δa respectively. The ratio between b and c determines how close the method is to a displacement control or a force control ($b/c = \infty \rightarrow$ force control and $b/c = 0 \rightarrow$ displacement control).

The scaling matrix A was created to be $K_0^T K_0$, where K_0 is the tangent stiffness matrix at initial condition (unloaded). In this case, $K_0^T = K_0$ since the matrix K_0 is symmetric. By applying the scaling matrix A to the displacement increment, both component of the arc-length have the same physical meaning (in this case force). Depending on the nature of the problem, sometimes it is much more efficient to use the current tangent stiffness matrix K at each step. However, it was not necessary in this case since it yielded good convergence results.

In order to obtain a matrix equation of solving unknown displacement Δ, a truncated

Taylor series was applied on Equation 3.38

$$\begin{aligned}\left(d\Delta\frac{\partial}{\partial d\Delta}+d\lambda\frac{\partial}{\partial\delta\lambda}\right)f(\delta\Delta_n,\delta\lambda_n)&=\delta a-f(\delta\Delta_n,\delta\lambda_n),\\ f(\delta\Delta_{n+1},\delta\lambda_{n+1})=f(\delta\Delta_n,\delta\lambda_n)+\frac{\partial f}{\partial\delta\Delta}d\Delta+\frac{\partial f}{\partial\delta\lambda}d\lambda&=\delta a.\end{aligned} \tag{3.39}$$

Then through algebraic manipulation one can obtain

$$f(\delta\Delta_n,\delta\lambda_n)=\frac{c(\lambda\Delta_n)^TA\Delta_n+b\delta\lambda_n^2}{f(\delta\Delta_n,\delta\lambda_n)}. \tag{3.40}$$

Taking partial derivative of $f(\delta\Delta_n,\delta\lambda_n)$ with respect to Δ and λ respectively one can get

$$\begin{aligned}d\Delta\frac{\partial}{\partial\delta\Delta}f(\delta\Delta_n,\delta\lambda_n)&=\frac{c}{f(\delta\Delta_n,\delta\lambda_n)}\delta\Delta_n^TAd\Delta,\\ d\lambda\frac{\partial}{\partial\delta\lambda}f(\delta\Delta_n,\delta\lambda_n)&=\frac{b}{f(\delta\Delta_n,\delta\lambda_n)}\delta\lambda_nd\lambda.\end{aligned} \tag{3.41}$$

Then by rewriting the above equations into matrix form, it finally yields

$$\begin{bmatrix}K & F^e\\ \frac{c}{f}\delta\Delta_n^TA & \frac{b}{f}\delta\lambda_n\end{bmatrix}\begin{bmatrix}d\Delta\\ d\lambda\end{bmatrix}=\begin{bmatrix}-F\\ \delta a-f\end{bmatrix}. \tag{3.42}$$

Note that the above equation is evaluated at step $(\delta\Delta_n,\delta\lambda_n)$ and (Δ_n^i,λ_n^i). The initial value of $\delta\Delta_0$ and $\delta\lambda_0$ at each step is set as the same value as the convergence value from the previous step. Since the "previous step" does not exist for the very first step, $\delta\lambda_0=\delta a$ and $\delta\Delta_0=K_0^{-1}F_0^e\delta\lambda_0$ is chosen to initialize the analysis, which yield a good approximation based on [Wiebe, 2012].

3.3.3 Newmark-Beta Time Integration Method

Nonlinear dynamic systems are often too complex to solve directly with closed-form solutions. Numerical methods have been developed for a long time to solve such problems. One important classification of numerical methods is explicit versus implicit. Implicit methods find the solution by solving equations involving the current state of the system and the later one, therefore it's unconditionably stable no matter what the time step size is. However, the step of inverting the stiffness matrix at each step adds a lot of computational cost. Compared to implicit method, explicit methods usually have much less computational cost, but stability problems may occur when time step is large.

In this section implicit integrator the Newmark-beta method is chosen to solve the beam vibration under buckling configuration for the reason that unnecessary intractably small time steps would be needed if using implicit method. The Newmark-beta method was developed in [Newmark, 1959] to solve large scale nonlinear system of equations in structural dynamics. Below is a general algorithm for the method.

Consider a system of equations that is yielded from the co-rotational finite element beam model as below

$$M\ddot{\Delta} + C\dot{\Delta} + F^{int}(\Delta) = F^{ext}(t), \tag{3.43}$$

where M, C, $F^{int}(Q)$, and $F^{ext}(t)$ respectively represent mass matrix, damping matrix, nonlinear internal force, and external force. Then the Newmark-beta update from t_n to t_{n+1} is shown as below

$$\begin{aligned}
\Delta_{n+1} &= \bar{\Delta}_{n+1} + \beta dt^2 \ddot{\Delta}_{n+1}, \\
\dot{\Delta}_{n+1} &= \bar{\dot{\Delta}}_{n+1} + \gamma dt \ddot{\Delta}_{n+1}, \\
\bar{\dot{\Delta}}_{n+1} &= \dot{\Delta}_n + (1-\gamma) dt \ddot{\Delta}_n, \\
\bar{\Delta}_{n+1} &= \Delta_n + dt\dot{\Delta} + \frac{1-2\beta}{2} dt^2 \ddot{\Delta}_n,
\end{aligned} \tag{3.44}$$

where the constant γ and β are parameters associated with the quadrature scheme. $\gamma = 1/2$ and $\beta = 1/4$ are used in the analysis because the algorithm provides a second order accuracy and is unconditionally stable in this case. The equation of motion can finally be obtained using the above equations as

$$F(\Delta_{n+1}) = \bar{K}\Delta_{n+1} + F^{int}(\Delta_{n+1}) - F^{ext}(t_{n+1}) + C\bar{\dot{\Delta}}_{n+1} - \bar{K}\bar{\Delta}_{n+1} = 0, \tag{3.45}$$

where $\bar{K} = (M + \gamma dtC)/(\beta dt^2)$. The tangent stiffness matrix is given by $K = \bar{K} + \nabla F^{int}$, where one can find that the second component is identical to the tangent stiffness matrix obtained in the static analysis. Within each step, the Newton-Raphson method is used instead of arc-length method since there are no turning point involved.

3.4 Results and Comparison

An analytical model and a numerical model were built using the methods described above. A bifurcation curve can be obtained from static analysis to trace what the mid-point displacement is for each compressive axial force value. The result plots are shown as below in Figure 3.5:

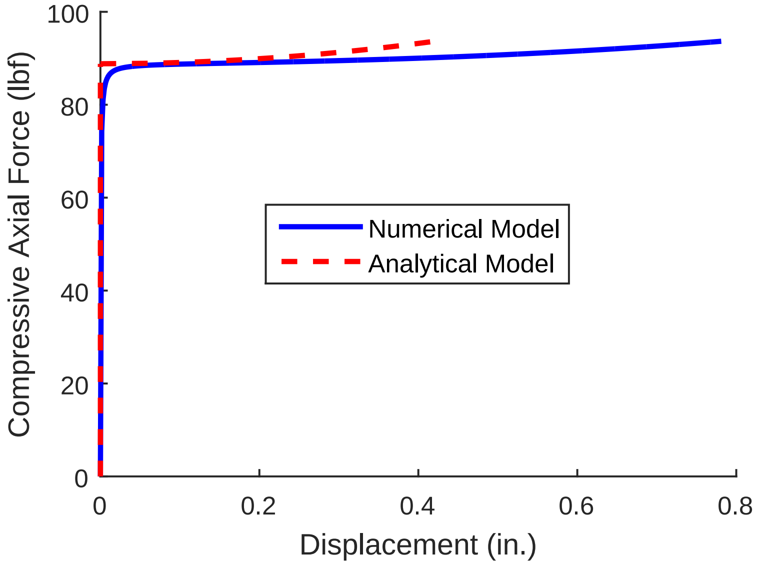

Figure 3.5: Bifurcation curves

The analytical model and the numerical model showed a high consistency of the buckling load (approximately 88.2 lbf) and within small displacement region. Note that the analytical model is derived under the assumption that the beam is inextensible. Thus when large displacement occurs, the beam tends to behave stiffer than it actually is. Another reason that might cause the inaccuracy of the analytical model is that all the Tayler expansions are applied about mid-point displacement equals to zero, which may cause errors when there are large displacements.

Theoretically, buckling phenomenon would not occur if there is no imperfection. If a beam is perfectly straight and is only under compressive axial loading, the failure mode would be crushing instead of buckling. Therefore, an initial imperfection was added to the numerical model. Note that in order to save computational cost, the b/c ratio mentioned in Section 3.3.2 is changed to be much smaller after buckling point so that the arc-length method behaves closer to a load control method within pre-buckling region and a displacement control method within post-buckling region.

Then applying dynamic analysis using Newmark-beta method, one can obtain the natural frequencies of the beam under different compressive axial force. Below in Figure 3.6 shows a comparison between the analytical model and the numerical model of the relationship between the first natural frequency squared, f_1^2, and the compressive axial force, P.

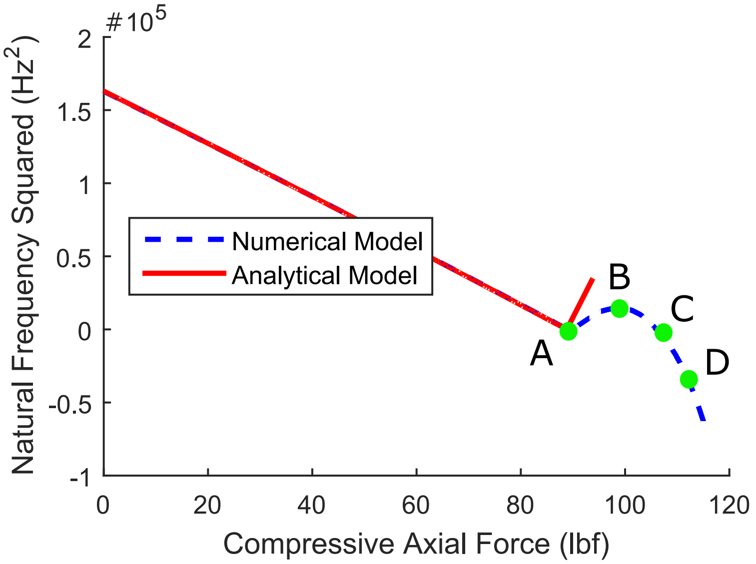

Figure 3.6: The effect of buckling load on beam natural frequency

As it can be observed from Figure 3.6 that the curves are right on top of each other before the compressive axial force reaches buckling load (approximately 88.2 lbf). However, the numerical model no longer shows a linear relationship between f_1^2 and P in post-buckling region unlike the analytical model, which indicates a linear relationship with a doubled slope from pre-buckling to post-buckling region. In numerical model, the f_1^2 even reaches a negative value when the compressive axial force gets to approximately 107 lbf, which indicates that it reaches to an unstable region.

The deformed shape of the beam corresponding to the loading condition A (buckling point), B (limit point of the first natural frequency squared), C (solution form change point from stable to unstable), and D (a random point in unstable region) as it shown in Figure 3.6 are also plotted in Figure 3.7 to Figure 3.10 respectively. It can be observed that when the solution form goes from stable to unstable, the beam has already shortened approximately 35 percent.

Note that the boundary conditions are quite tricky in the numerical code when analyzing the natural frequency under buckling configuration. For example, when under a vertical motion to the mid-point of the beam, the allowance of the horizontal motion of one end would make it much easier to trigger the first mode motion. Thus the fixed-fixed buckling beam as is shown in ($b1$) is much stiffer than the fixed-roller buckling beam as is shown in ($c1$). The same analogy goes with a pin-pin beam and a pin-roller beam as is shown in ($b2$) and ($c2$) as well. As it is illustrated in Figure 3.12, whether the horizontal degree of freedom of one end is fixed or not does not affect the first natural frequency value until it reaches the buckling load. The one with fixed-fixed boundary condition shows a huge jump of the natural frequency when it reaches the buckling load as compared to the fixed-roller one shows a similar relationship between the f_1^2 and P with the analytical model. The same behavior of comparison also applies to pin-pin versus pin-roller boundary condition as is shown in Figure 3.13. If the squared second and third natural frequencies of a pin-pin beam versus the compressive axial force are plotted, as is shown in Figure 3.14, it is observed that the jump of the squared natural frequency when buckling occurs is from the first natural frequency to the second natural frequency. This is because when the horizontal degrees of freedom are fixed at both ends, it would be easier to trigger the second mode shape than the

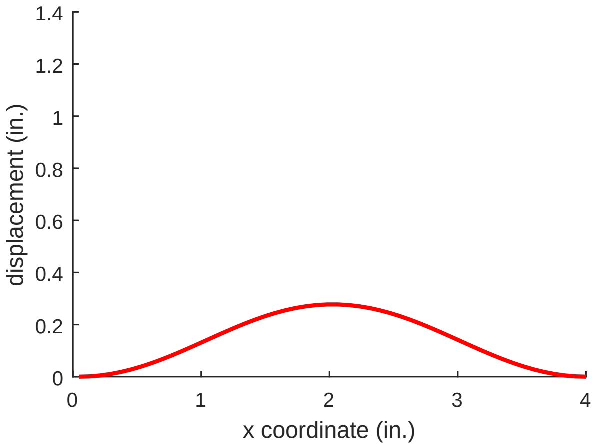

Figure 3.7: Point A configuration

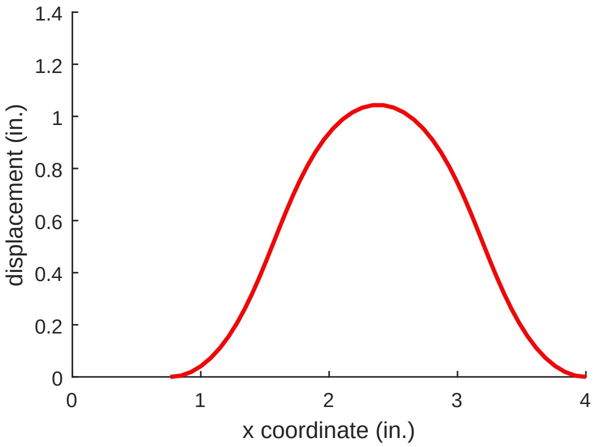

Figure 3.8: Point B configuration

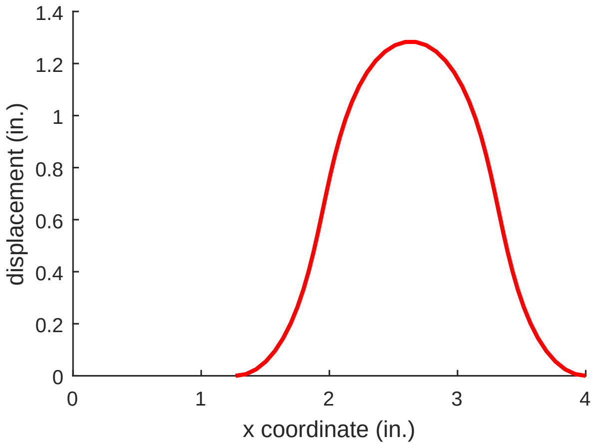

Figure 3.9: Point C configuration

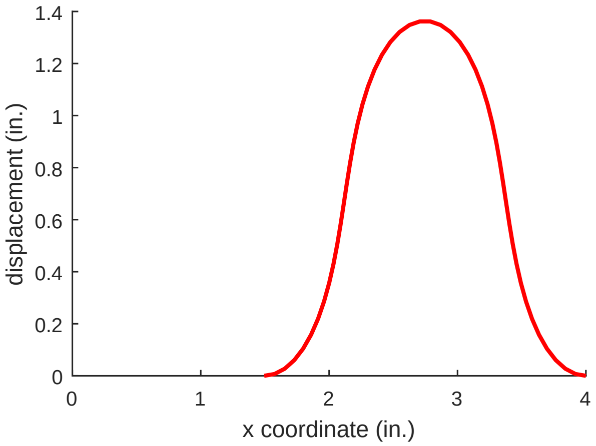

Figure 3.10: Point D configuration

first one.

It is worth mentioning that the analytical model does not have such issue because it is assumed the distance between the end nodes remains approximately as the original length in Equation 3.7. So theoretically, the analytical model actually has a fixed-roller boundary condition as it shown in ($c1$) of Figure 3.11.

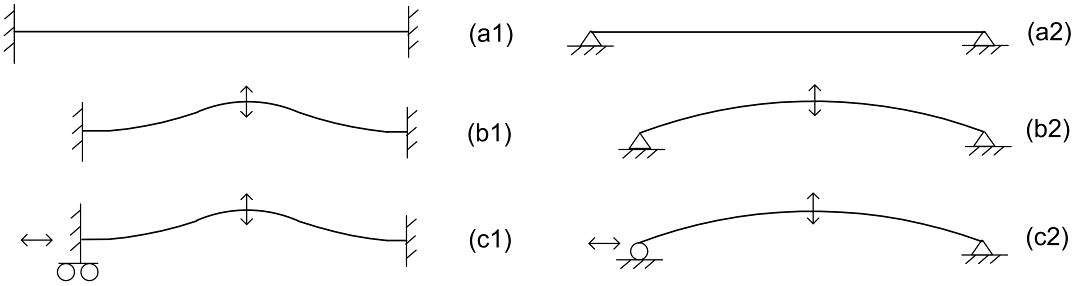

Figure 3.11: Boundary conditions under buckling configuration

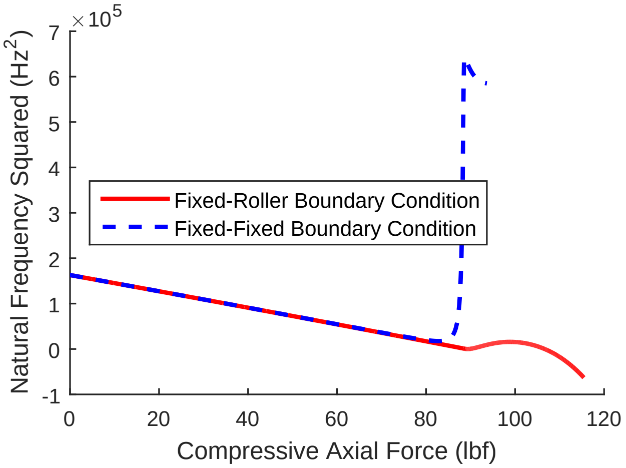

Figure 3.12: Fixed-fixed versus fixed-"fixed-roller"

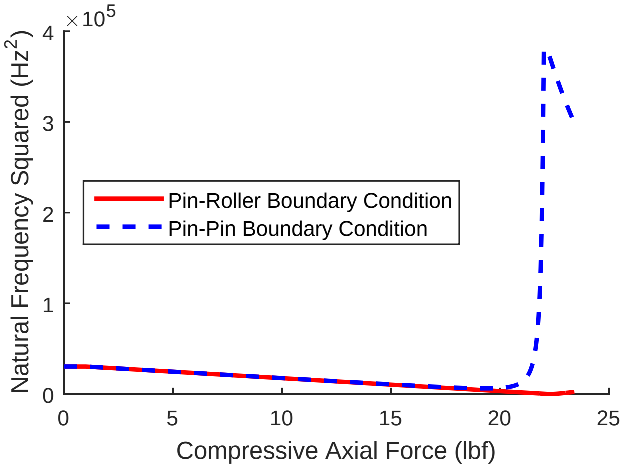

Figure 3.13: Pin-pin versus pin-roller

3.5 Remarks and Conclusion

In this chapter, an analytical model and a numerical model were presented for the static and dynamic analysis for beam vibration under buckling configuration. It is concluded that in the pre-buckling region, the relationship between the first natural frequency squared and the compressive axial force remains linear as it described in Chapter 2. The analytical model shows that after buckling load, the relationship between the two still remains linear, however the absolute value of the slope of the curve is doubled. The relationship between the two obtained from the numerical model no longer remains linear after reaching the buckling load.

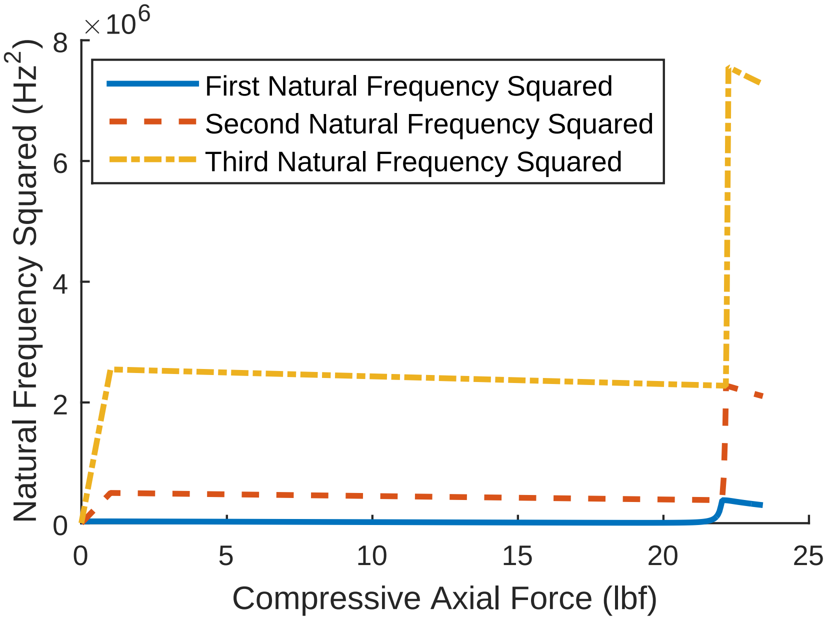

Figure 3.14: Square of the first three natural frequencies versus compressive axial force

It is softened until it becomes unstable (complex natural frequency). Due to the inconsistent behavior between the numerical model and the analytical model, it is suggested that future experimental work should be conducted to better understand how buckling affect the natural frequency of a beam. Another interesting found is the sensitivity of natural frequency to the boundary conditions. Frequency jumps (from first one to the second one, the second one to the third one, and so on) were found from the numerical model when assigned with perfect fixed-fixed or pin-pin boundary conditions. However, such extreme boundary conditions rarely exist in real world.

Chapter 4

YIELDING - BEAM VIBRATION UNDER TENSILE AXIAL FORCE

4.1 Introduction

The eigenparameters are really important in the application of nondestructive health monitoring of structural elements as a cost-effective way to detect the existence of damage and its extent. Literature studies have shown a numerous amount of research that successfully identified damage on different structural elements and systems based on changes in natural frequencies, such as beams with various boundary conditions [Kim, 2003; Khiem and Toan, 2014; Yuen, 1985] and cables [Lepidi et al., 2009]. However, most of the research has focused on how cracking affect natural frequencies of the element. Very little research has be done in terms of how natural frequency changes within yielding and strain hardening regions (specifically steel structures).

In Chapter 2, the linear relationship between the squared first natural frequency and the axial force within the linear elastic beam vibration region has been discussed. What follows in this chapter is the effect of yielding on the relationship between the two, which was investigated both experimentally and numerically, and its application in nondestructive health monitoring of steel beams.

4.2 Experiments

The same test specimens and the experimental setup were used as is described in Section 2.4. The test procedure is as follows:

4.2.1 Test Procedure

This experiment is an extension to the test described in Chapter 2. The first three steps in Section 2.4.2 were repeated in this experiment. Then the following steps were followed.

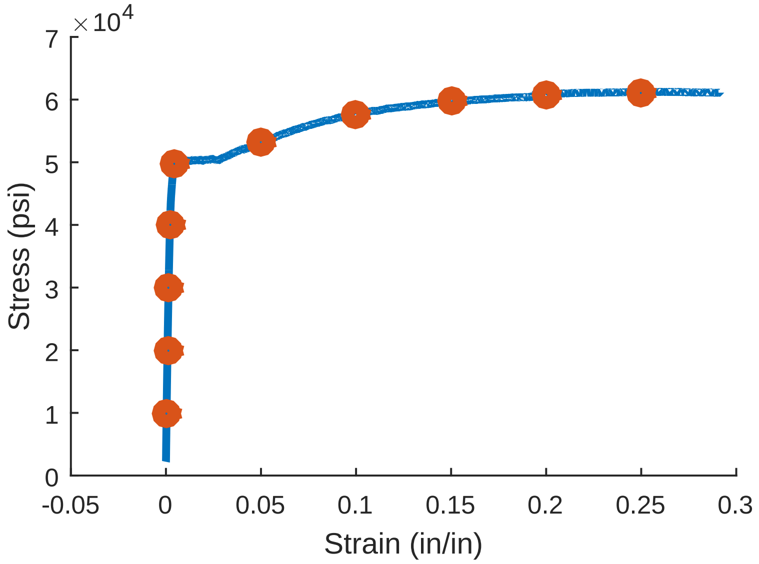

Figure 4.1: Test points illustration

As is shown in Figure 4.1, a load control method was used to obtain the first five points within the linear elastic region. Then the process was switched to a displacement control technique, since the axial load does not vary significantly initially after yielding. A strain increment of 0.05 was used to obtain different test points as is shown in Figure 4.1.

For each test point, the loading was paused when it reached the desired strain value in order to obtain the first natural frequency under different plastic deformation. A frequency sweep was performed and the mid-point displacement history was recorded using the displacement sensor. Since it is nearly impossible to start the frequency sweep and the displacement sensor at the exact same time, one should start the displacement sensor and record the time, t_{start}, of when the frequency sweep is applied.

Note that the deformed length of the specimen was measured for each test point since length is one of the main factors that affect the natural frequency. However, it is the stiffness, which can be reflected from the natural frequency value, that is of primary concern in this research. Thus it is important to know the change of other parameters that affect the natural frequency so that they can be normalized at the end.

4.2.2 Results and Analysis

Two specimens were tested following the above procedure. As is shown in Figure 4.2 the stress-strain relationship for the test specimen 2, when pausing the tensile loading within the plastic region, the load dropped at each point due to the loading mechanism in the Instron machine.

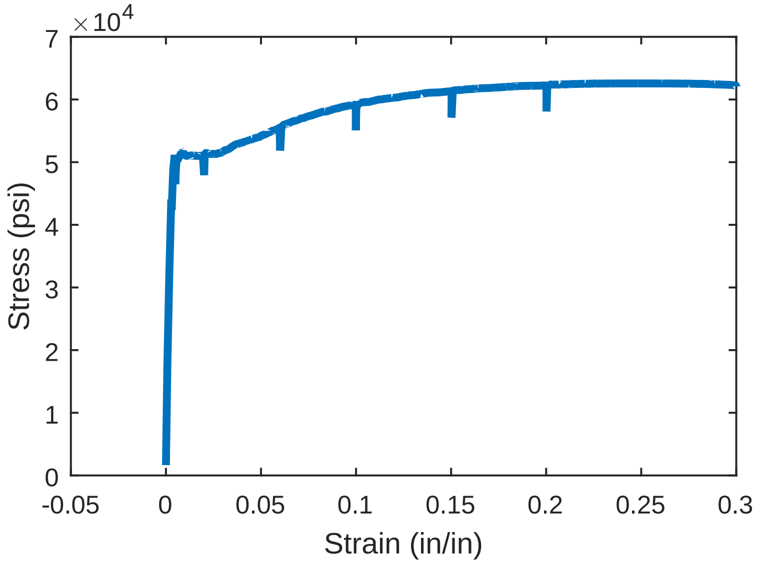

Figure 4.2: Stress-strain relationship for the test specimen 2

In order to get a amplitude-frequency curve from the displacement history under a frequency sweep, the angular frequency values were calculated using equation $f_i = a + bt$, where a is the initial applied frequency and b is the sweep rate. As for the corresponding displacement amplitude, the amount of data, n, from the displacement history for each frequency value can be calculated using $n = b/T_{sensor}$, where T_{sensor} represents the displacement sensor

Table 4.1: Test results for the effect of plastic deformation on the natural frequency

Specimen 1				Specimen 2			
Region	Tension, lbf	Natural frequency, Hz	Effective length, in	Region	Tension, lbf	Natural frequency, Hz	Effective length, in
Linear Elastic	20	117.05	8.25	Linear Elastic	17	114.05	8.25
	282.5	314.75	8.25		160	237.15	8.25
	419	379.35	8.27		286	310.15	8.25
	531	423.45	8.28		406	367.15	8.26
	582	442.45	8.29		493	411.35	8.27
Yield	601	448.35	8.42	Yield	594	453.85	8.28
Strain hardening	650	450.65	8.48	Strain Hardening	612	443.85	8.41
	689	447.45	9.07		666	445.75	8.73
	716	440.95	9.49		704	442.55	9.05
	728	431.85	9.9		724	437.65	9.45
	731	403.35	10.73		739	422.25	9.85
	-	-	-		746	408.45	10.29
	-	-	-		745	393.05	10.65

measuring rate. Then the amplitude approximately equals to the average of the maximum and minimum of the n number of the displacement data points chosen. Obtaining the natural frequency value as the same forcing frequency value corresponding to the maximum displacement amplitude, the results are as shown in Table 4.1.

The effect of the plastic deformation on the relationship between the squared first natural frequency and the axial force can be shown as plotted in Figure 4.3. Both specimens show a clear softening behavior after they reach the yielding point. However, as is shown in Table 4.1, the elongation of the specimens is significant within the plastic region. An approximately 30 percent elongation was reached by the end of the test for both specimens. As is discussed in previous chapters, the natural frequency is proportional to $1/L$. Thus the squared first natural frequency values were normalized by a factor of L^2. As is plotted in Figure 4.4, the squared first natural frequency values were normalized by P/L^2 to ensure that theoretically it would be a straight horizontal line within the linear elastic region.

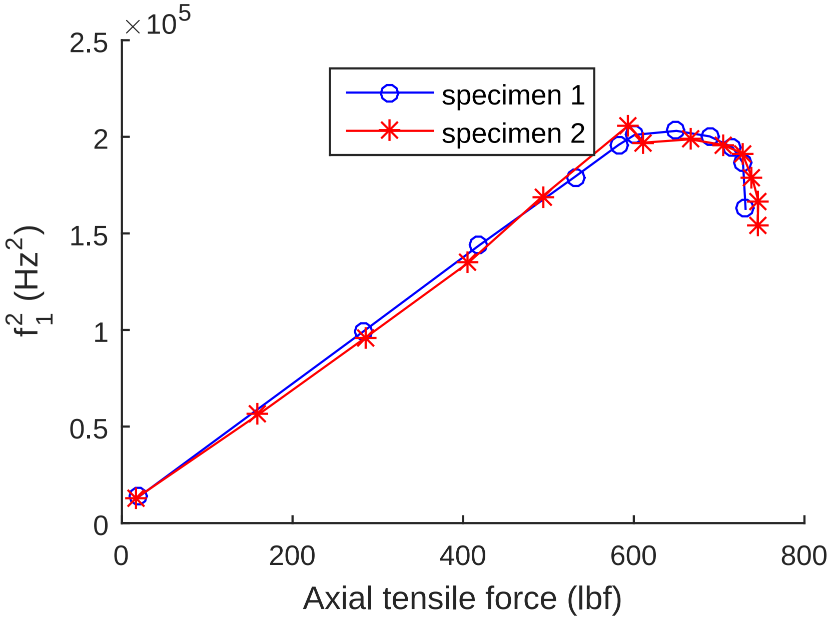

Figure 4.3: The relationship between the squared first natural frequency and the axial tensile force

As is shown in Figure 4.4, as expected, specimen 1 shows an approximately horizontal linear relationship between the normalized squared first natural frequency and the axial force within the elastic region. Specimen 2 shows a slight increase of the normalized squared first natural frequency value, which might be caused from machine and measuring errors. However, both specimens indicate a sudden drop from the yielding point to the first point within the strain hardening region and then an increase of the normalized squared first natural frequency value after that.

It can be concluded that some of the softening behavior within the plastic region as is

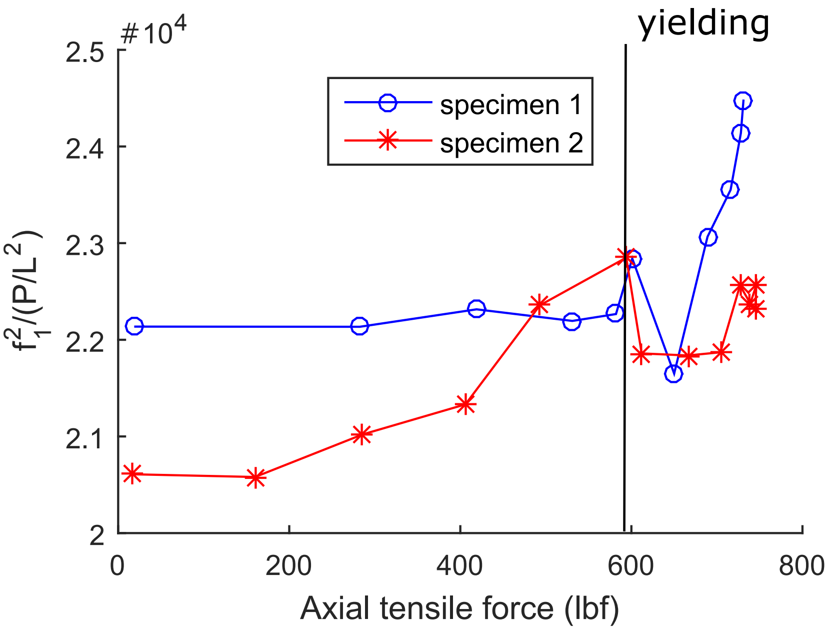

Figure 4.4: The relationship between the normalized squared first natural frequency and the axial tensile force

shown in Figure 4.3 could be caused by the elongation of the specimen. From the material point of view, the stiffness hardening can be observed from Figure 4.4. The small drop of the normalized squared first natural frequency value from the yielding point to the first point in strain hardening region is more difficult to explain. In order to better understand the result, it is first important to know what the stiffness value represents in this experiments. As is shown in Figure 4.5, when the beam is axially loaded at the yield load, the extreme top and bottom fibers at the mid-point of the beam, point A and point B, are under equal tensile stress, as is shown in the stress-strain relationship at the top left of the figure. Then when the beam oscillates transversely under driving, the extreme tension fiber, point A, sees increasing strain and the extreme compression fiber, point B, experiences unloading as is shown at the top middle of the figure. When the beam oscillates back to its original straight configuration as is shown in at the top right of the figure, point A, experiences unloading back to the same stress value as point B experienced in the last step, as point B experiences loading up to yield stress. When point A becomes the extreme compression fiber and point B becomes the extreme tension fiber, point B reaches to the same position as point A was, and point A experiences unloading as is shown at the bottom left of the figure. Eventually, point A and point B would just switch their position (from the stress-strain plot) as is shown at the bottom right of the figure. Therefore the stiffness represents the initial unloading stiffness in this experiment. Note that the illustration above is approximate because the neutral axis position would keep changing through the vibration. However, it would eventually reach to a state as is shown in the bottom right of the figure, which represents that the beam is actually vibrating within the elastic region. In order to further validate that the vibration within the plastic region was still a beam behavior instead of a string behavior, which means that it loses its bending stiffness, a natural frequency comparison between the experimental results and a theoretical analysis of a string, which has the same parameters as the test specimen, was plotted as is shown in Figure 4.6.

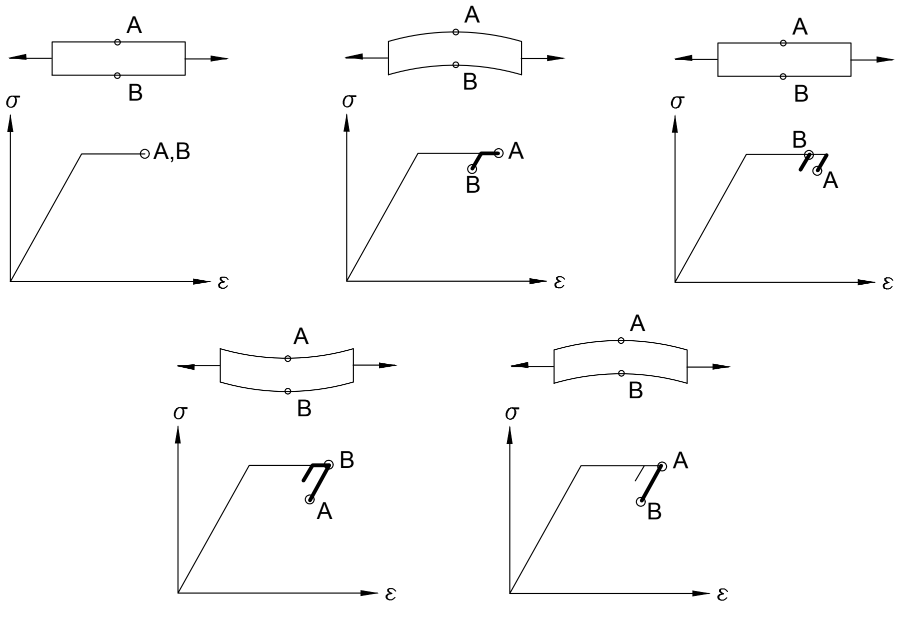

Figure 4.5: Illustration of beam vibration under axial tension

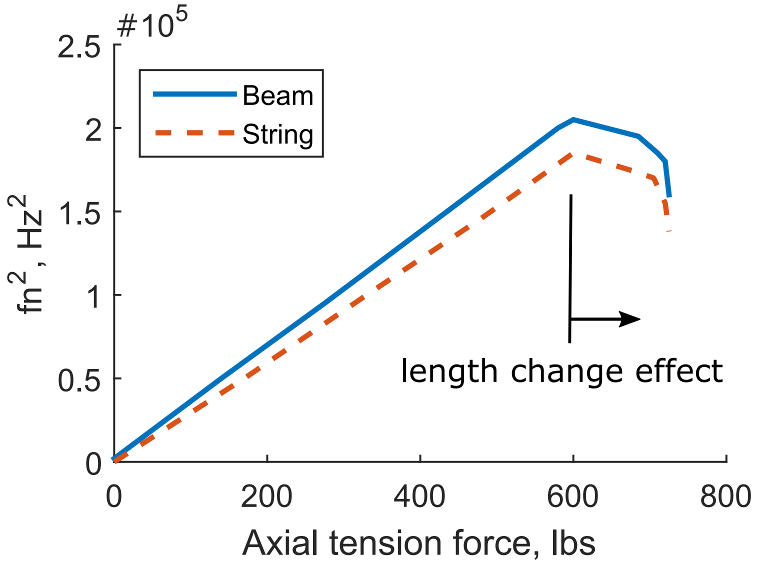

Figure 4.6: Comparison between beam and string behavior

The experimental results indicate a smaller unloading stiffness when the specimen first reaches the plastic region and an increasing unloading stiffness within the strain hardening region compared to the initial stiffness. The reason behind the results remains unclear. Future experiments on both hot rolled steel and cold rolled steel are needed in order to better understand this phenomenon.

4.3 Numerical Model

When modeling steel elements including material nonlinearity, most of the current researchers whether used a lumped plasticity model, for example as is described in [Mazza and Mazza, 2010], or developed a stiffness reduction matrix, for example as is described in [Ngo-Huu et al., 2007], in order to capture the nonlinear behavior. In this work, an elastic-plastic finite element model was developed to thoroughly study the static and dynamic behavior of a steel beam under plastic deformation.

4.3.1 Quasi-Static Analysis

Model Description

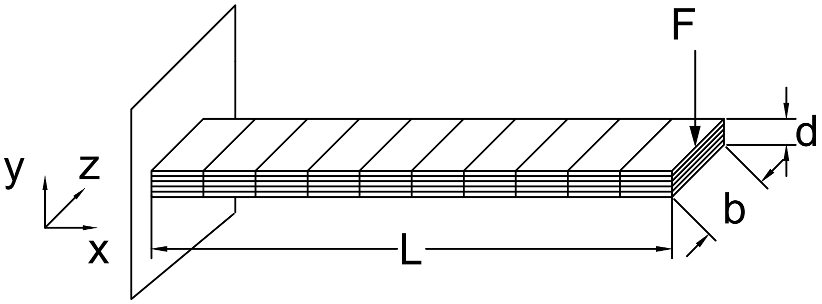

Figure 4.7: Schematic illustration of the plasticity model for a cantilever beam

In order to validate the workability and the accuracy of the distributed plasticity model, a cantilever beam was analyzed. As it can be seen in Figure 4.7, the specimen was discretized into n elements in the x direction and m elements in the y direction. The z direction deformation can be neglected thus the specimen was not meshed in that axis.

The purpose of the distributed plasticity model is to better understand the effect of the plastic deformation on the natural frequency values. And therefore, geometric nonlinearity is not considered in this model due to the small displacement amplitude. It is also assumed that plane sections remain plan during the analysis, which may be a poor estimate.

A bi-linear isotropic steel material model was initially used for the analysis. As is explained later in the algorithm section, different material models can be easily implemented into this analysis if needed.

Analysis Algorithm

Note that only the general algorithm is discussed in this section. Since it is a quasi-static analysis, the target of the algorithm is to find the displacement under a given applied load. An incremental analysis is used to save computational time since the applied force changes smoothly.

At the start of each step, the change of the applied force, ΔF_{ext}, should be defined. Based on a static analysis of the cantilever beam, the incremental moment value, ΔM_n, for each horizontal node, n, can be calculated with the known nodal coordinates. For each point x, an iteration process is needed to find out which incremental curvature value would lead to the target incremental moment. One should start the initial guessing of the curvature, ϕ_n, as zero and use a very small curvature increment for each step, which should have the same sign as ΔF_{ext}. Within each iteration, for a given curvature value ϕ_n, the strain for each vertical component can be calculated since the neutral axis is located at the middle of each horizontal component (no axial force) and a linear strain distribution is assumed (plane sections remain plane).

The next step, which is the key component of the analysis, is to calculate the vertical stress distribution for each element. This is where the material nonlinearity is included. As mentioned, a bi-linear stress-strain relationship as is shown in Figure 4.8 is used for the analysis. It is essential to keep track of the stress and strain history, and the residual strain value, $\epsilon_{residual}$, for each element of the specimen. This is especially important when the model is subjected to a cyclic loading. The residual strain should only be updated using Equation 4.1 when there is a turning point (the sign of the force changes, for example, point A) and the absolute value of the stress has already passed the yield stress, σ_y, within the loading cycle (between the last turning point and the current one).

$$\epsilon_{residual} = \frac{E_1 \epsilon_t - \sigma_t}{E_1}, \tag{4.1}$$

where ϵ_t and σ_t respectively represents the strain and the stress value of the turning point when $\epsilon_{residual}$ is updated. Then one can calculate the current step incremental stress value, $\Delta\sigma_{nm}$ (the incremental stress value for horizontal node n and vertical node m), corresponding

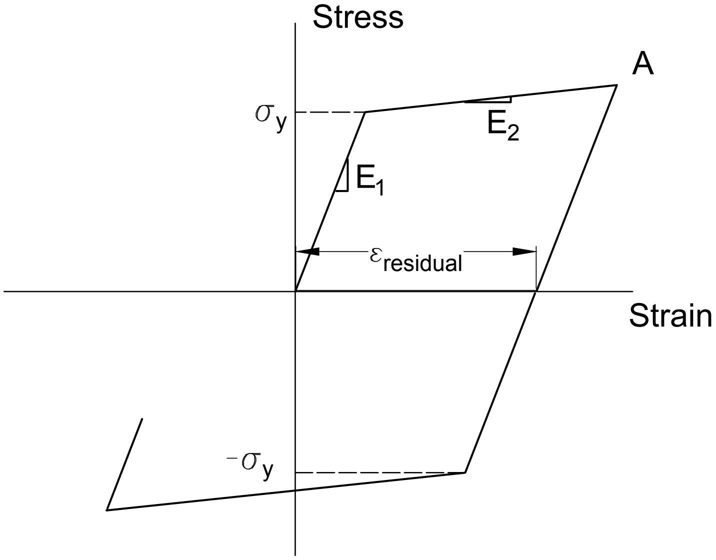

Figure 4.8: Illustration of the stress-strain relationship in the distributed plasticity model

to the current step incremental strain value, $\Delta\epsilon_{nm}$, using the following equations:

$$\begin{aligned} \Delta\sigma_{nm} &= E_1\Delta\epsilon_{nm} \quad \text{if} \quad \text{abs}\{(\Delta\epsilon_{nm}+\epsilon_{nm,i-1})E_1\} < \sigma_y \\ &\phantom{= E_1\Delta\epsilon_{nm}} \quad \text{or} \quad \text{sign}(\Delta\epsilon_{nm}+\epsilon_{nm,i-1}) = \text{sign}(\epsilon_t) \\ \Delta\sigma_{nm} &= E_1\Delta\epsilon_{nm} \quad \text{else}, \end{aligned} \tag{4.2}$$

where $\epsilon_{nm,i-1}$ is the strain value from the previous step. Then the corresponding moment value for element n, $\Delta M_{n,trial}$, can be calculated as:

$$\Delta M_{n,trial} = \sum_{j=1}^{m} \sigma_{nm} b y_m \frac{d}{m}, \tag{4.3}$$

where y_m is the distance from the center of element m to the bottom of the specimen. Then one should compare $\Delta M_{n,trial}$ with the target incremental moment value, ΔM_n. Iterations are needed until the different between $\Delta M_{n,trial}$ and ΔM_n is smaller than the defined tolerance. Finally, when the targeted ΔM_n values are reached, the incremental displacement of node n, Δv_n, can be calculated by numerically integrating the curvature twice. Note that after each integration the value at the fixed end would be a non-zero value. Since there should be no displacement at the fixed end, all the calculated values after each integration should be normalized by adding the difference between the fixed-end value and zero. Then the system properties at the current step can be updated using:

$$\begin{aligned} v_{n,i} &= v_{n,i-1} + \Delta v_n \\ \sigma_{n,i} &= \sigma_{n,i-1} + \Delta \sigma_n \\ \epsilon_{n,i} &= \epsilon_{n,i-1} + \Delta \epsilon_n . \end{aligned} \tag{4.4}$$

Analysis Results

A convergence study was conducted in the elastic region to investigate the number of horizontal nodes needed in the static analysis. As is shown in Figure 4.9, the tip displacement is already really close to the convergence value when there are only 15 horizontal nodes. The value finally converged with 35 horizontal nodes with a tip displacement of 0.1048 in. Note that the tip displacement can be calculated with the theoretical equation $v = FL^3/3EI$ when it is within elastic region, which gives a displacement value of 0.11 in. Compared to the theoretical result, the numerical result has a 4.5% error. Note that in order to achieve better result, a convergence study of the amount of vertical nodes should also be conducted and it is still ongoing currently.

A large amplitude cyclic loading was applied to test the distributed plasticity model. As is shown in Figure 4.10, a sinusoidal force was applied at the tip of the beam. The result plot of the tip displacement response is illustrated in Figure 4.11. The nonlinear behavior can be observed. Also, from the 1^{st} cycle to the 5^{th} cycle of the sinusoidal force, the displacement of the tip reduced under the same applied force. This is caused by the strain hardening behavior from the bi-linear material model. It can also be obtained that when the tip reached the largest displacement value at the first cycle, as is shown in Figure 4.12, 14.35% of the elements were in plastic region (highlighted region).

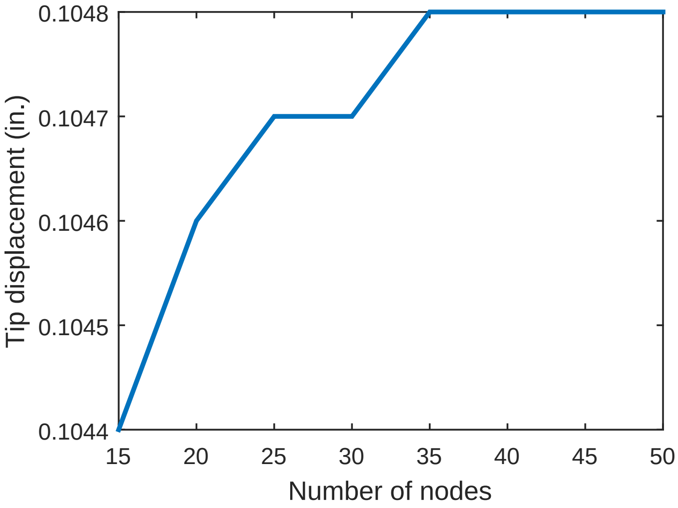

Figure 4.9: Convergence study for the horizontal node number in static plasticity model

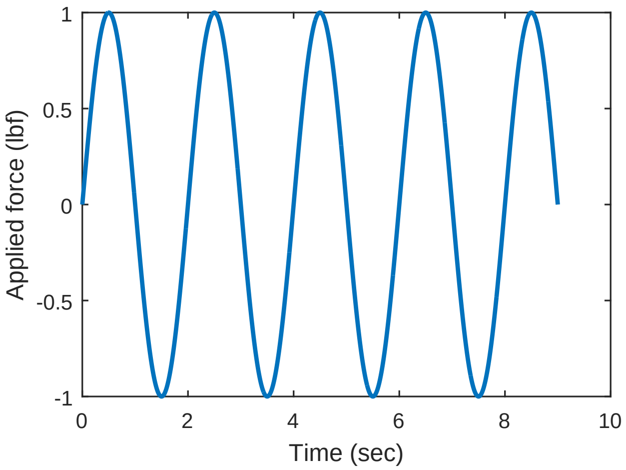

Figure 4.10: Applied force

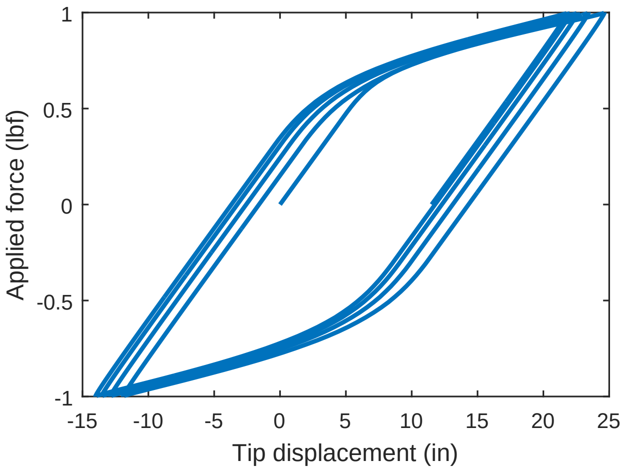

Figure 4.11: Force-displacement history

4.3.2 Dynamic Analysis

The mesh of the finite element model and the material properties are kept the same as the quasi-static analysis. However, the algorithm can no longer be used because for dynamic analysis, the moment distribution for each time step can no longer be directly calculated. What follows in this section is the general algorithm of the dynamic analysis and a description

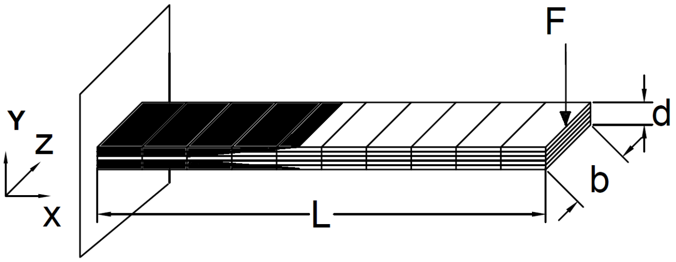

Figure 4.12: Illustration of the yielded element

of the time-integration method used in the analysis.

4^{th} *Order Runge-Kutta Time Integration Method*

The 4^{th} order Runge-Kutta method is a very well established time integration method. For a general first order ODE system $v'(t) = f(t, v(t))$, the time step update of the classical RK4 is given by:

$$v_{n+1} = v_n + h\left[\frac{k_1}{6} + \frac{k_2}{3} + \frac{k_3}{3} + \frac{k_4}{6}\right], \tag{4.5}$$

where h is the step size, and

$$\begin{aligned} k_1 &= f(t_n, v_n) \\ k_2 &= f(t_n + \frac{h}{2}, v_n + \frac{h}{2}k_1) \\ k_3 &= f(t_n + \frac{h}{2}, v_n + \frac{h}{2}k_2) \\ k_4 &= f(t_n + h, v_n + hk_3). \end{aligned} \tag{4.6}$$

As it can be observed from the above equations, the 4^{th} order Runge-Kutta method is a single-step method with four stages per step. It does not require derivatives of the function f in the analysis, which is the reason why this method was chosen over Newmark method for the dynamic analysis of the distributed plasticity finite element model. However, a very small time step should be used in order to keep the stability of the analysis.

Analysis Algorithm

Note that only the general algorithm is discussed in this section.

As derived in Chapter 2 Equation 2.20, the equation of motion for a beam under transverse force without axial loading (the one with axial loading considered will be discussed later) can be expressed as:

$$EI\frac{\partial^4 v}{\partial^4 x} + \mu\ddot{v} + \beta\dot{v} = F_{trans}(x,t). \tag{4.7}$$

However, if a nonlinear material model is used, the term M'' can no longer be represented by $EI\frac{\partial^4 y}{\partial^4 x}$. Thus the equation of motion for the dynamic analysis for the plasticity model becomes:

$$M'' + \mu\ddot{v} + \beta\dot{v} = F_{trans}(x,t). \tag{4.8}$$

In order to apply the 4^{th} Runga-Kutta method to solve the system equation, the equation of motion can be expressed with the following equations:

$$\begin{aligned} \dot{v} &= \dot{v} \\ \ddot{v} &= \frac{1}{\mu}\left(F_{trans}(x,t) - M'' - \beta\dot{v}\right). \end{aligned} \tag{4.9}$$

Then for each step, one needs to update displacement, v, and velocity, $\dot{v}$, for each horizontal element. The difference between the dynamic analysis and static analysis is that the moment value for each horizontal element can no longer be directly calculated for a given applied force. For each stage within a time step, the moment value should be calculated based on the previous step displacement. First, the curvature can be calculated by taking the double derivative of the displacement using central difference method, which can be expressed as:

$$\phi_n = \frac{v_{n-1} - 2v_n + v_{n+1}}{(L/n)^2}. \tag{4.10}$$

Note that for the boundary nodes whether the term v_{n-1} or the term v_{n+1} would not exist. Thus an imaginary point needs to be created as is illustrated in Figure 4.13. For a fixed end, the imaginary point should have a displacement the same as the adjacent node of the fixed end node so that it provides a smooth curve with approximate zero rotation at the boundary. For a free end, zero curvature should be assigned since there is no moment.

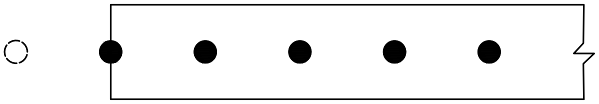

Figure 4.13: Illustration for the imagined point at the boundary ends

The strain value for each element, ϵ_{nm}, can be calculated from $\epsilon_{nm} = \phi_n c_m$, where c_m is the distance from the center of element m to the center of the whole horizontal element. Then the process of calculating the stress from the strain and the moment from the stress is the same as is described in the quasi-static analysis procedure. To complete the calculation of k_v (i.e. $\dot{v}$), M'' can be calculated using central difference method. For a fixed end, the M'' does not need to be evaluated since there should be no displacement or velocity at the fixed node. It is meaningless to update the slope of velocity at that point. For a free end, an imaginary point with a moment value equal to the adjacent point to the boundary node should be created since the shear (first derivative of moment) is zero at a free end.

Within each step, the above calculation process should be repeated for four times with updated displacement and velocity in order to calculate the slope values k_{1v}, k_{2v}, k_{3v}, k_{4v}, $k_{1\dot{v}}$, $k_{2\dot{v}}$, $k_{3\dot{v}}$, $k_{4\dot{v}}$. Finally the current step displacement and velocity can be updated using:

$$\begin{aligned} v_i &= v_{i-1} + h\left[\frac{k_1 v}{6} + \frac{k_2 v}{3} + \frac{k_3 v}{3} + \frac{k_4 v}{6}\right] \\ \dot{v}_i &= \dot{v}_{i-1} + h\left[\frac{k_1 \dot{v}}{6} + \frac{k_2 \dot{v}}{3} + \frac{k_3 \dot{v}}{3} + \frac{k_4 \dot{v}}{6}\right]. \end{aligned} \tag{4.11}$$

Note that for a fixed end boundary condition, the nodal displacement should be manually input as zero after each step.

Analysis Results

In order to test the distributed plasticity model, a cantilever model was tested under a large magnetic force, which was described in Section 2.4. A large amplitude sinusoidal force was applied for three seconds, then the force was removed so that the beam allowed to exhibit free decay. Figure 4.14 shows the tip displacement of the cantilever model. When zooming in the displacement history from 18.5 second to 20 second as is shown in Figure 4.15, it can be observed that even though the beam was still oscillating, it was oscillating about a non-zero displacement. Thus plastic deformation at the fixed end must have been caused.

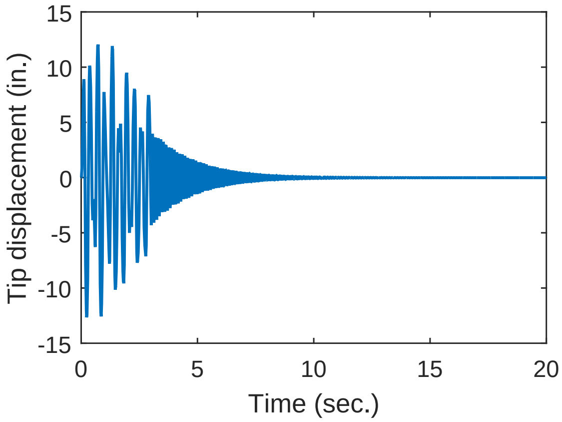

Figure 4.14: Displacement history for the tip point of the cantilever model

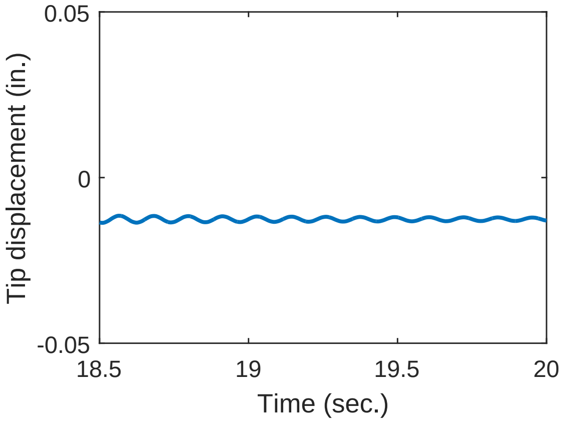

Figure 4.15: Zoomed in displacement history for the last 1.5 second

Finally, a fixed-fixed beam with the same dimensions and material properties as the experimental specimens was tested using the dynamic distributed plasticity model. In order to test the accuracy of the plasticity model, a beam vibration within linear elastic region was tested to compare with the result from the analytical model described in Chapter 2. An magnetic force with parameters $a = L/2$, $d = 1/8$ in., $k = 0.024$, and $\omega = 20$ rad/sec, was applied on the specimen. A convergence study was conducted and the results are as shown in Figure 4.16. The converged numerical result of the mid-point displacement of the specimen is almost approximately 50% larger than the analytical result. The reason for this error is still under investigation. One possible reason of the large displacement is that it is really difficult to implement the boundary conditions correctly to the dynamic model. With the current algorithm, the overall deformed shape is reasonable as is shown in Figure 4.17. However, when zooming in on the fixed end as is shown in Figure 4.18, zero rotation is not achieved at the boundary. The current algorithm fixed the boundary by manually applying a zero displacement value at the fixed node and implementing an imaginary displacement point that has a same value as the adjacent node of the fixed end, which provides a large rotational stiffness. However, it does not provide an infinite rotational stiffness as it should have for a fixed boundary condition. Thus future studies are needed to improve the model.

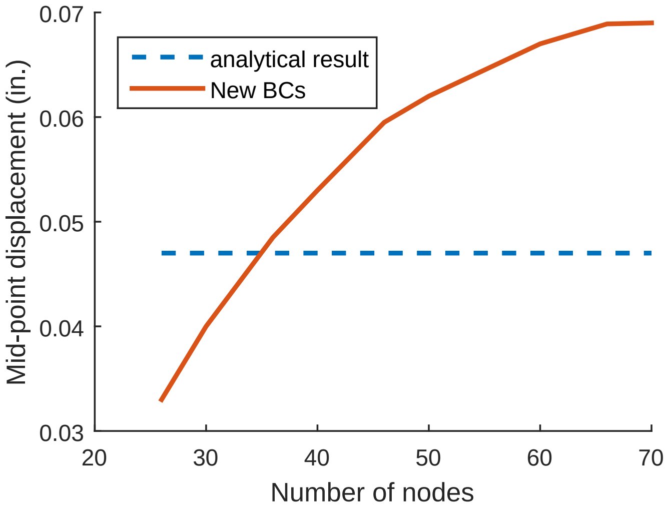

Figure 4.16: Convergence study for the horizontal node number in dynamic plasticity model

4.4 Conclusions and Future Work

In this chapter, the effect of yielding and strain hardening on the relationship between the squared first natural frequency and the axial force of beams was studied experimentally. Initially a softening behavior was captured from the plot within the plastic region. However, after normalized the first natural frequency value with L^2, it is found that the stiffness was

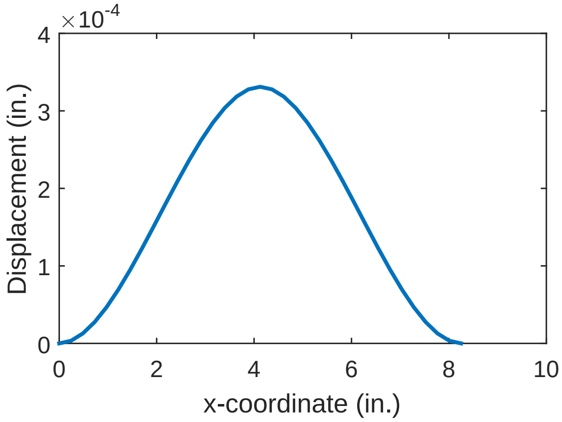

Figure 4.17: Deformed beam configuration

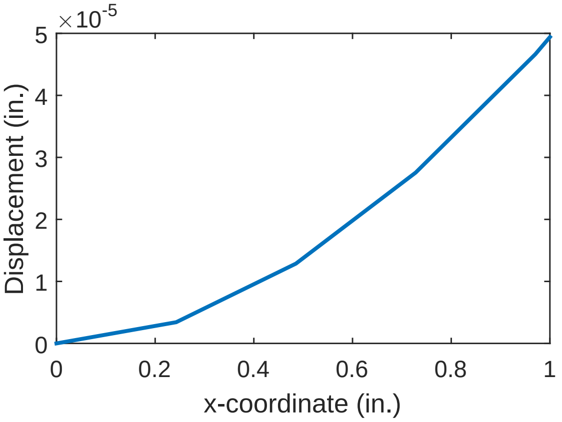

Figure 4.18: Zoomed in deformed shape at fixed end

actually hardened within the plastic region. It was observed that for both test specimens the normalized first natural frequency value dropped from the yielding point to the first point in strain hardening region. The hypothesis was made that it was caused by the local yielding, which was originated from the yielding plateau in the stress-strain relationship. However, in order to validate the theory, more tests need to be done in the future on both hot-rolled steel beams, which shows a clear plateau in the stress-strain relationship, and cold-rolled steel beams, which does not have a plateau region in the stress-strain relationship.

A numerical model was also developed in this work to investigate the effect of plastic deformation on the natural frequencies. The workability of the distributed plasticity model was proved by both quasi-static analysis and dynamic analysis. The accuracy of the displacement response for the quasi-static analysis was also validated. However, the dynamic analysis of the model still needs to be improved in the future. Eventually the model should include the axial force effect to the distributed plasticity model since the main purpose of the model is to study the beam natural frequency under axial plastic deformation. A general algorithm of implementing the axial force into the model is provided as follows.

When adding the axial force effect to the algorithm, the equation of motion becomes:

$$M'' + Qv'' + \mu\ddot{v} + \beta\dot{v} = F_{trans}(x,t). \tag{4.12}$$

The equation of motion can be rewritten into the below system of equations so that the 4^{th} order Runge-Kutta method can be applied:

$$\begin{aligned} \dot{v} &= \dot{v} \\ \ddot{v} &= \frac{1}{\mu}\left(F_{trans}(x,t) - M'' - Qv'' - \beta\dot{v}\right). \end{aligned} \tag{4.13}$$

The main difference between the analyses with axial force and without axial force is the neutral axis location. In the previous algorithm, the neutral axis was at the center of the element, thus it is very straightforward to calculate the strain values from the known curvature. However, with axial force, the neutral axis potentially changes each step. In order to solve this problem, iteration process of the neutral axis location is needed. For each step, one should iterate the neutral axis location to match the axial force and moment simultaneously. Then one can use the same process of calculating strain, stress, and moment within each step with known curvature and neutral axis. However, an extra step of calculating the total force acting on the element from the stress values should be added. The axial force calculated should equal to the applied axial force, otherwise one should keep iterating the neutral axis location.

Chapter 5

THE EFFECT OF YIELDING ON BEAM RE-LOADING STIFFNESS

5.1 Introduction

In the previous chapters the effect of axial force on the natural frequency of a beam was investigated. The stress-strain curve of the tested A366/1008 steel used in this study is shown in Figure 5.1. The natural frequency of the beam under a tensile axial force, for example at point A, reflects the stiffness of the beam when applying an infinitesimal motion under the same configuration. However, oftentimes a beam or a beam-like element is under cyclic loading condition. Thus in this work, the effect of large tensile axial force (plastic deformation) on the re-loading stiffness of a beam was also investigated experimentally in order to develop a robust steel material model.

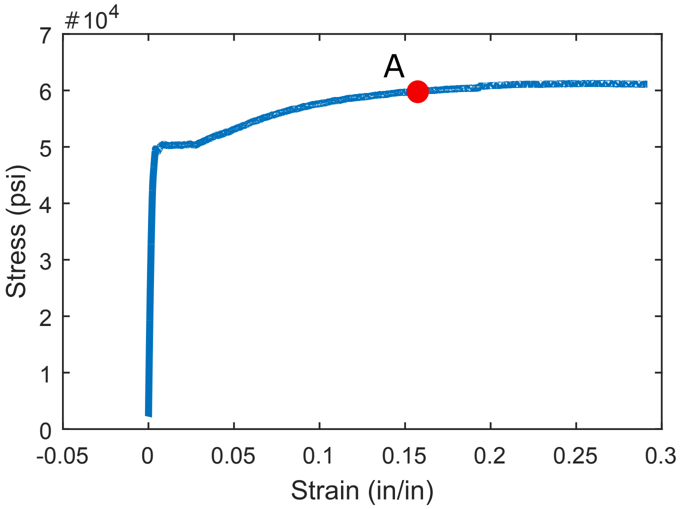

Figure 5.1: Stress-strain relationship of A366/1008 steel from experiments

In most studies, steel under cyclic loading is modeled with a bi-linear stress-strain relationship with isotropic strain hardening as it shown in Figure 5.2 or a Giuffre-Menegotto-Pinto model with isotropic strain hardening as it illustrated in Figure 5.3. Other models were also developed based on these two models, however almost all of them assumed a constant Young's modulus during reloading no matter whether plastic deformation is developed or not until the start of the 21^{st} century. Several authors indicated that the Young's modulus of some metals decreased when plastic deformation occurred and detected up to 15% deduction of the Young's modulus in steels, aluminum, copper, and brass [Roca et al., 2014].

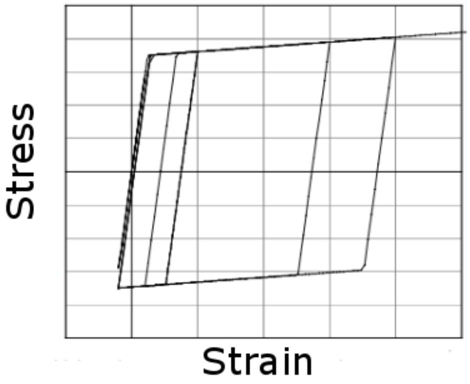

Figure 5.2: Bi-linear steel model with isotropic strain hardening [Mazzoni, 2012]

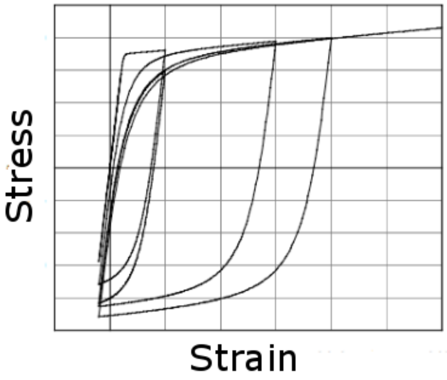

Figure 5.3: Giuffre-Menegotto-Pinto model with isotropic strain hardening [Mazzoni, 2012]

A great review of how plastic deformation affect Young's modulus of different metallic alloys can be found in [Roca et al., 2014]. In his work, the results of the Young's modulus of UNS G10180 and UNS G10430 steels measured during loading and unloading steps in tension test were presented as it shown below in Table 5.1. It can be observed that the reduction of Young's modulus is approximately from 15% to 20% once the plastic deformation occurs while the percentage of the reduction has no clear relationship to the amount of the plastic deformation from these experimental data.

Table 5.1: The effect of plastic deformation on the Young's modulus of steel [Roca et al., 2014]

UNS G10180 Steel				UNS G10430 Steel			
Step	Plastic Strain, (%)	*	E, (GPa)	Step	Plastic Strain, (%)	*	E, (GPa)
1	0.0 - 0.9	L U	206 172	1	0.0 - 1.0	L U	204 167
2	0.9 - 2.2	L U	210 170	2	1.0 - 2.3	L U	208 159
3	2.2 - 3.2	L U	200 165	3	2.3 - 3.0	L U	202 161
4	3.2 - 4.3	L U	208 171	4	3.0 - 3.9	L U	206 164
5	4.3 - 5.6	L U	202 179	5	3.9 - 5.2	L U	193 165
6	5.6 - 8.0	L U	204 183	6	5.2 - 6.9	L U	183 160
7	8.0 - 9.5	L U	197 178	7	6.9 - 7.8	L U	195 163
8	-	- -	- -	8	7.8 - 9.0	L U	180 160

[*] Note: L, measurement during initial loading;
U, measurement during unloading.

5.2 *Experiments*

In this work, experiments were conducted to further investigate the effect of plastic deformation on Young's modulus.

5.2.1 Experiment Setup

Instron 600DX, a material testing machine as it shown in Figure 5.4, was used to provide axial tensile loading and unloading condition in this experiment. Instron 600DX is designed for high-capacity tension, compression, bending, and shear testing, which has a capacity range of 600 kN $(135,000 \text{ lbf})$.

Both cold rolled steel and hot rolled steel were tested in this experiment. Standard steel coupons with a 2 in. gauge length and a 0.5 in. diameter as it is defined in ASTM E8/E8M [ASTM, 2015] were used as test specimen. Below Figure 5.5 shows a deformed hot rolled A36 steel coupon after tension test.

5.2.2 Test Procedure

Note that of all the test procedure below the strain reading was obtained from an extensometer instead of the direct strain reading from the Instron Machine. This is because the Instron Machine strain calculation considers the original length as the distance between the two platform instead of the two grips, which represents the effective length of the specimen.

Step 1. Tension Test

A standard tension test based on ASTM E8/E8M [ASTM, 2015] should be performed to get a stress-strain curve of the test specimen so that the load of interests could be selected evenly spaced along the curve. Record the yield strength and the peak strength of the test specimen.

Figure 5.4: Instron 600DX

Figure 5.5: Deformed coupon after cyclic tensile axial loading

Step 2. Measurement of Young's modulus when loading and unloading within elastic region

Add tensile axial load to the specimen until it reaches approximately half the yield force. Record the stiffness (initial Young's modulus) as a control value. Unload, then reload to the same axial force for three times. Record the stiffness after reloading each time. This is done so to study how axial force (within elastic region) affect the Young's modulus.

Step 3. Measurement of Young's modulus when loading and unloading within plastic region

After the third time reloading to approximately half the yield force. Keep loading until it just reaches the yield force. Unload, then reload to the same axial force for three times. Record the stiffness after reloading each time. This is done so to study how yielding affects Young's modulus. Then perform the same type of cyclic loading and record corresponding

Young's modulus for an axial load point that is half way between the yield strength and the peak strength and for the peak strength point in order to study the relationship between the percentage of reduction (if there is any) of Young's modulus and the amount of plastic deformation. Note that the same loading rate throughout the test should be used as it is defined in ASTM E8/E8M [ASTM, 2015].

Step 4. Measurement of Young's modulus when loading to the specimen's peak strength and unloading

Since all of the specimens above have undergone cyclic loading (different degree of plastic deformation) before they reach their peak strength. There may be some uncertainty in the relationship between the amount of plastic deformation and the percentage of reduction of Young's modulus. In this step, the specimen should be loaded directly to the peak strength, record the initial stiffness (Young's modulus). Unload, then reload to the same axial force for three times. Record the stiffness after reloading each time.

Note that even though more plastic deformation can be obtained after the specimen reaches the peak strength, especially for hot-rolled steel, the specimen tends to fail in a brittle way after cyclic large tensile loading (i.e. cold worked). Thus the failure load is unpredictable and sudden. For the safety of the extensometer, one should not go further than the peak strength when perform the same test.

5.2.3 Test Results and Analysis

Followed the test procedure listed above, two hot-rolled A36 steel and two cold-rolled steel coupon were tested and the results are as follows in Table 5.2 and Table 5.3. The results of a hot-rolled A36 steel coupon followed by *Step* 4 is also presented below in Table 5.4.

Table 5.2: Hot-rolled steel test results

Hot-Rolled Steel Specimen 1				Hot-Rolled Steel Specimen 2			
	Group	E, (ksi)	% Decrease		Group	E, (ksi)	% Decrease
Initial E	1	30650	0	Initial E	1	29740	0
Elastic Region, 30 ksi	2	30590	0.196	Elastic Region, 30 ksi	2	30470	-2.455
	3	30330	1.044		3	30420	-2.286
	4	31000	-1.142		4	30566	-2.777
Just yield, 56 ksi	5	26825	12.480	Just yield, 56 ksi	5	29149	1.987
	6	28676	6.440		6	28581	3.897
	7	27512	10.238		7	29339	1.348
First point after entering plastic region, 63 ksi	8	27609	9.922	First point after entering plastic region, 63 ksi	8	28946	2.670
	9	27668	9.729		9	28179	5.249
	10	27677	9.700		10	27757	6.668
Peak strength, 77 ksi	11	27632	9.847	Peak strength, 77 ksi	11	29357	1.288
	-	-	-		12	29320	1.412
	-	-	-		13	28496	4.183

Table 5.3: Cold-rolled steel test results

Cold-Rolled Steel Specimen 1				Cold-Rolled Steel Specimen 2			
	Group	E, (ksi)	% Decrease		Group	E, (ksi)	% Decrease
Initial E	1	30000	0	Initial E	1	32755	0
First point in plastic region, 60 ksi	2	24354	18.82	First point in plastic region, 60 ksi	2	27021	17.506
	3	24662	17.793		3	26983	17.622
	4	25534	14.887		4	27142	17.136
Peak strength, 71 ksi	5	24514	18.287	Peak strength, 71 ksi	5	28342	13.473
	6	23000	23.333		6	28240	13.784
	7	24089	19.703		7	27400	16.349

Table 5.4: Hot-rolled steel test results 2

	Group	E, (ksi)	% Decrease
Initial E	1	29700	0
Peak Strength, 76 ksi	2	27311	8.044
	3	28184	5.104
	4	27884	6.114

As it can be observed from the results tables, hot-rolled steel, as expected, shows no reduction in Young's modulus within elastic region. When plastic deformation occurs, except for a few data points from specimen 2, all other results indicate a reduction of Young's modulus from 5% to 10%. The cold-rolled steel shows a reduction of the Young's modulus of approximately 15% to 20% under plastic deformation, which matches closely with the previous experiments conducted by [Roca et al., 2014].

5.3 Remarks and Conclusion

In this chapter, the effect of plastic deformation on the Young's modulus of steel was discussed. Both experiments from this work and recent literature conclude that there's a clear reduction in Young's modulus (different degree of reduction for hot-rolled steel and cold-rolled steel) when plastic deformation occurs. This information can be used as a damage detection method to predict whether a structural component had ever undergone plastic deformation in the past, for instance, after an earthquake. The difficulty, however, would be estimating the boundary conditions correctly. Also, there is no clear relationship between the amount of plastic deformation and the percentage of reduction of Young's modulus. This is of great concern for structural engineers, because most steel material models used in numerical analyses and commercial software assume a constant Young's modulus under all loading types. When there is a large reduction of Young's modulus in a structural member, the behavior of a structural system would be greatly affected, particularly in cases of severe cyclic loading, like that of a large earthquake. The displacement under the same loading would be much higher with a reduced Young's modulus, which should be of concern especially for a drift-controlled design procedure.

For future work, more tests should be done to investigate the material behavior of structural steel under extreme cyclic loading.

Chapter 6

LARGE AMPLITUDE VIBRATION

6.1 Introduction

In previous chapters the relationship between the axial force and the square of natural frequency of beam vibration within different regions (linear elastic, buckling, yielding and strain hardening regions) has been investigated using a well-rounded approach between analytical methods, numerical methods, and experiments. However, all the conclusions from above methods are built upon the assumption that the displacements are small. In reality, large forces may lead to large deformations and hence nonlinear response in the modeling of beam or beam-like elements. Its application includes not only structural elements in civil, mechanical, and aerospace engineering, but even in biomaterials. For example, Miller [2005] conducted theoretical research on the effects of hardening (elastic modulus increases with strain) and softening (elastic modulus decreases with strain) nonlinearities on the structural dynamics of plant stems in order to prevent high stress occurring along the stem and root system.

Figure 6.1 (a) shows a chematic force-displacement curve without geometric nonlinearity. Respectively, the amplitude-frequency curve for a stiffness hardening system and a stiffness softening system is shown in Figure 6.1 (b) and (c), respectively.

Hardening and softening resonance curves are caused by large force amplitude induced geometric nonlinearity. A cantilever beam, as an example of a stiffness hardening system, is illustrated in Figure 6.2. When a small amplitude force is applied as is shown in (a), it can be assumed that $F_{axial} \approx 0$, and thus the stiffness can be expressed as $k = k_{bending} = 3EI/L^3$. However, the larger the force is, the larger the axial component of the force becomes. For most structures, axial stiffness $k_{axial} = AE/L$ is much greater than the bending stiffness

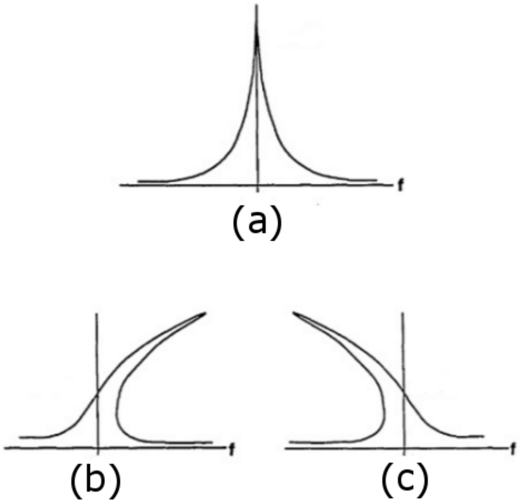

Figure 6.1: Schematic amplitude-frequency curves for hardening and softening resonance [Mallow and Lucas, 1992]

$k_{bending}$. Therefore the stiffness is "hardened" when a large amplitude force is applied.

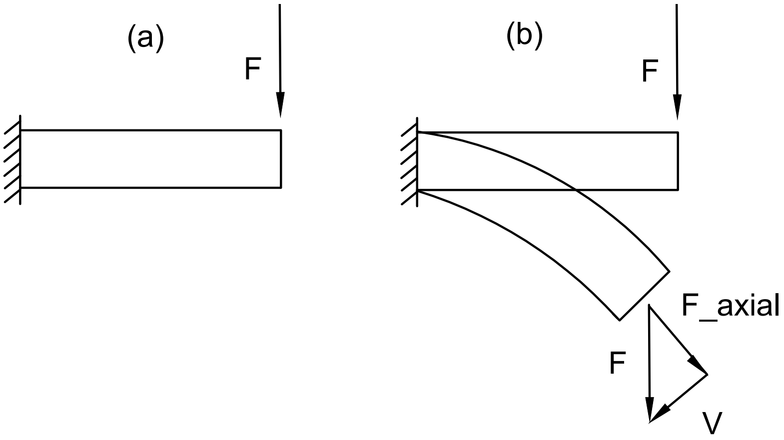

Figure 6.2: Large force amplitude cantilever vibration

The large amplitude vibration of beams has been studied by researchers using both analytical and numerical methods for a long time. A good review can be found in Das et al. [2011]. A numerical analysis of large amplitude beam vibration under different boundary conditions and excitation patterns is also presented in this paper. Large amplitude nonlinear vibration has drawn numerous researchers' attention for the reason that it is sometimes detrimental to have large amplitude vibration (resonance) occurring under an unexpected forcing frequency.

In performing the vibration experiments discussed in the other chapters, some interesting nonlinear response was discovered. This chapter will introduce those results. Additionally, the work is intended to serve as a reminder of the difficulties of ensuring linear response, as the original nonlinear behavior was accidentally observed in tests that were intended to be linear.

6.2 Experiments

Experiments were done by the researcher studying the amplitude-frequency curve of a fixed-fixed beam with large amplitude transverse harmonic force in order to validate the backbone curve developed in theory. The same experimental setup as is described in Section. 2.4 was used for this experiment.

6.2.1 Test Procedure

In order to achieve large deformation, zero axial force is added to the specimen. A step of obtaining the natural frequency of the specimen under zero axial force was performed using small amplitude frequency sweep as is described in *Step* 2 in Section. 2.4.2. Then an amplifier was used to amplify the voltage output in order to obtain a large amplitude force.

As is shown in Figure 6.1, it is nearly impossible to trace the curve experimentally using a frequency control method. However, an approximate curve can be obtained by running the large amplitude frequency sweep both forward and backward.

After plotting the amplitude-frequency curves from running large amplitude frequency sweep both forward and backward, one frequency point was chosen from the backbone curve to study if multiple stable vibration amplitudes can be obtained by adding an impact load.

6.2.2 Results and Analysis

A natural frequency of 72.5 Hz was obtained from a small amplitude frequency sweep test. Then large amplitude frequency sweeps with $a = 60$ Hz, $b = 0.2$ Hz/sec (b value comes from convergence test) and $a = 120$ Hz, $b = -0.2$ Hz/sec were applied on the specimen respectively. The displacement response history for both sweeps are as shown respectively in Figure 6.3 and Figure 6.4. It can be observed that the resonance behavior lasts much longer under the forward sweep than the backward sweep. Switching from time domain to frequency domain using the same technique as is described in previous chapters, the amplitude-frequency curves can be obtained as is plotted in Figure 6.5.

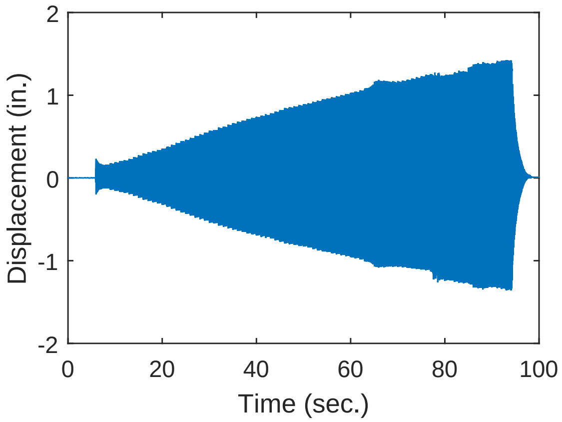

Figure 6.3: Displacement response history under large amplitude forward frequency sweep

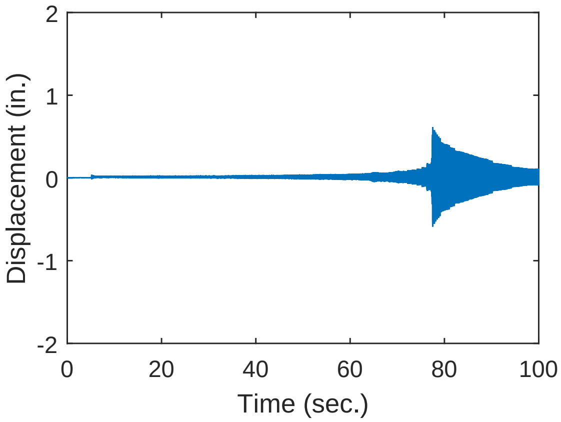

Figure 6.4: Displacement response history under large amplitude backward frequency sweep

The blue curve is the amplitude-frequency curve obtained from a forward large amplitude frequency sweep, and the orange one represents the backward sweep. As is shown in the figure, the vibration amplitude kept increasing after reaching the first natural frequency of the specimen (72.5 Hz) until 116 Hz when it suddenly dropped. However, when running the frequency sweep backward, the vibration amplitude stayed small until it reached the first natural frequency. Note that the red and blue curves do not match exactly for frequencies less than 72 Hz. Theoretically they should match exactly, but the error is probably within the

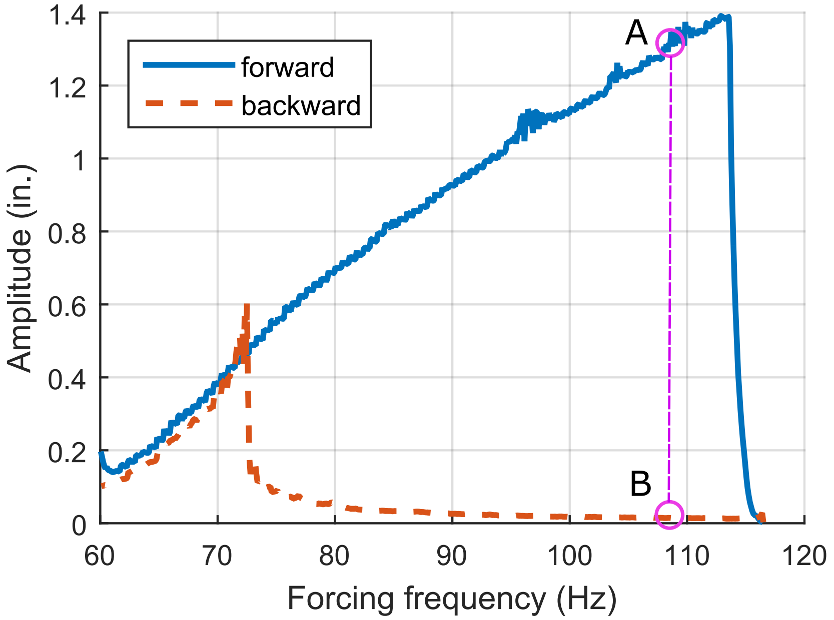

Figure 6.5: Amplitude-frequency curve for a fixed-fixed beam under large amplitude transverse force

possibilities of experimental repeatability and noise. Another irregular phenomenon is the bumped area around 96 Hz in the blue curve. When zooming in on this “bumped” region, the response contains two frequencies, which when approximated as shown in Figure 6.6 turn out to be $f_1 = 95.24$ Hz ($T_1 = 0.0105$ sec) and $f_2 = 3.57$ Hz ($T_1 = 0.28$ sec). This two frequency response means the amplitude of any given oscillation will lead to a somewhat ”bumpy” or irregular amplitude frequency plot.

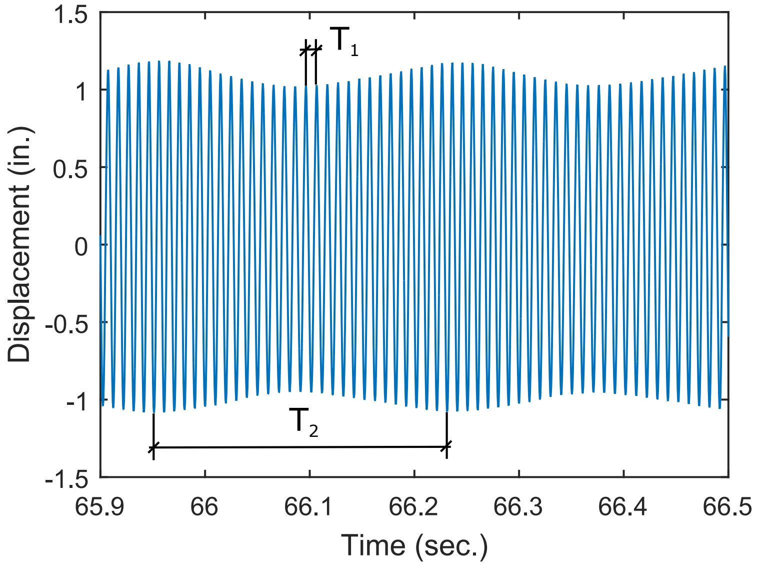

Figure 6.6: Displacement history for forcing frequency equal to 96 Hz

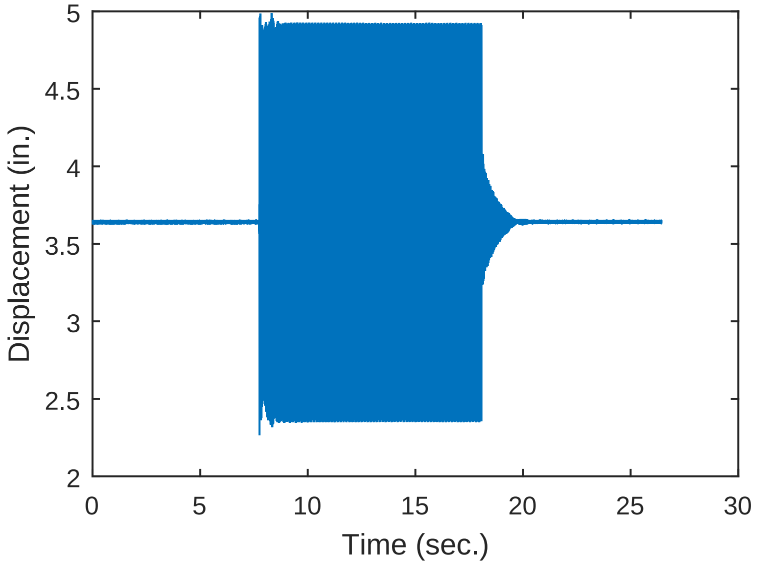

Figure 6.7: Amplitude jump

As is shown in Figure 6.7, the impact test result further validates the backbone curve by showing two stable vibration amplitudes under one forcing frequency (109 Hz was chosen). The specimen started with small vibration under a harmonic point load with a frequency of 109 Hz as is shown in Figure 6.5 as point B. Then an impact was applied, which resulted in an amplitude jump from a small amplitude vibration to a large one as indicated by point A. Finally another impact load brought the amplitude back to point B. If more frequency points were chosen, the real backbone curve would be defined more accurately.

6.3 Analytical Model

In this section a pin-pin beam will be investigated analytically to qualitatively (rather than quantitatively) validate the nonlinear hardening observed in the experiments. The pin-pin boundary conditions greatly simplify the analysis but still show a similar hardening trend caused by induced axial forces.

6.3.1 Equation of Motion

With large amplitude vibration, the axial stress caused by the deformation can no longer be neglected. Considering a discretized beam with an initial shape, $y_0(x)$, and a deformed shape, $y(x)$, as is shown in Figure 6.8, the curve length of a deformed beam can be expressed as

$$L_y = \int_0^L \sqrt{dx^2 + dy^2}\frac{dx}{dx} = \int_0^L \sqrt{1 + \left(\frac{dy}{dx}\right)^2} dx = \int_0^L \sqrt{1 + y'^{\,2}} dx. \tag{6.1}$$

Then the strain of the deformed beam, ϵ, can be calculated as

$$\epsilon = \frac{L_y - L_0}{L} = \frac{1}{L}\left(\int_0^L \sqrt{1 + y'^{\,2}} dx - \int_0^L \sqrt{1 + y_0'^{\,2}} dx\right). \tag{6.2}$$

Applying Taylor expansion to $\sqrt{1 + y'^{\,2}}$ at $y' = 0$ and neglecting higher order terms, one

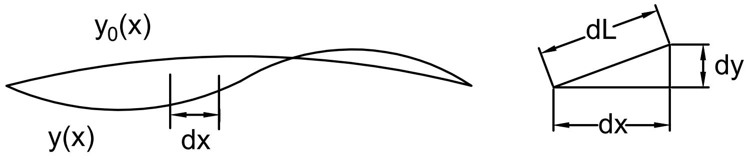

Figure 6.8: Illustration of a beam with large vibration amplitude

can obtain $\sqrt{1+y'^{\,2}} \approx 1+\frac{1}{2}y'^{\,2}$. Then the strain calculation can be simplified as

$$\begin{aligned}\epsilon &= \frac{1}{L}\left[\int_0^L (1+\frac{1}{2}y'^2)dx - \int_0^L (1+\frac{1}{2}y_0'^2)dx\right] \\ &= \frac{1}{2L}\left[\int_o^L (y'^2 - y_0'^2)\right].\end{aligned} \tag{6.3}$$

Finally, assuming an initially straight beam, the axial force caused by the large deformation, P_{de}, can be expressed as

$$P_{de} = EA\epsilon = \frac{EA}{2L}\int_o^L y'^{\,2}dx. \tag{6.4}$$

Note that the above formulation used a small strain assumption when solving a problem with large deformation. However, the accuracy of applying this formulation on solving displacement response under transverse force is proved by [Wiebe and Virgin, 2016] both experimentally and numerically when the ratio between the mid-point displacement and the length is smaller than 10%, which is certainly the case as the results shown in the next section.

Adding this term to Equation 2.20, one can obtain the equation of motion for a large amplitude beam vibration as

$$\mu\ddot{y} + \beta\dot{y} + EIy'''' + Qy'' = f(x,t), \tag{6.5}$$

where $Q = P - \frac{EA}{2L}\int_o^L y'^{\,2}dx$.

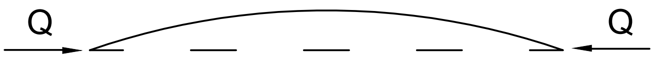

Figure 6.9: Axial force of a beam with large vibration amplitude

It is worth mentioning that the term P in Equation 6.5 was considered as the applied axial force by many previous researchers. However, as is shown in Figure 6.9, it is actually the term Q that represents the applied axial force. It is only true to state that $P = Q$ when there is no beam deformation. Physically speaking, P is what the axial force, Q, would be if beam deformation is not allowed.

6.3.2 Analytical Solution

In order to get the amplitude-frequency curve for a large amplitude beam vibration, a frequency sweep with a half sin spatial shape was applied, which can be represented as

$$f(x,t) = A(t)\sin\left(\frac{\pi x}{L}\right) \quad \text{where} \quad A(t) = \sin[(a+bt)t], \tag{6.6}$$

with a=initial angular frequency and b=sweep rate. Assuming the solution form $y = C(t)\sin(\pi x/L)$, it yields:

$$\begin{gathered}\mu\ddot{C}(t)\sin\frac{\pi x}{L} + \beta\dot{C}(t)\sin\frac{\pi x}{L} + EIC(t)\left(\frac{\pi}{L}\right)^4\sin\frac{\pi x}{L} - \\ PC(t)\left(\frac{\pi}{L}\right)^2\sin\frac{\pi x}{L} + C^2(t)\frac{\pi^2}{2L}\frac{AE}{2L}C(t)\left(\frac{\pi}{L}\right)^2\sin\frac{\pi x}{L} = A(t)\sin\frac{\pi x}{L}.\end{gathered} \tag{6.7}$$

This equation must hold true for all values of x, and thus the coefficients of the harmonics must balance to yield a single degree of freedom ordinary differential equation in time, which can be shown as:

$$\mu\ddot{C}(t) + \beta\dot{C}(t) + \frac{1}{\mu}\left(\frac{\pi}{L}\right)^2 \left(EI\left(\frac{\pi}{L}\right)^2 - P\right) C(t) + \frac{1}{\mu}\left(\frac{\pi}{L}\right)^4 \frac{AE}{4} C^3(t) = A(t). \tag{6.8}$$

If solving the same problem with a fixed-fixed boundary condition, the guessed solution form becomes $y = C(t)[1 - \cos(\pi x/L)]$ in order to satisfy the boundary condition, which leads to problem since the second time derivative of y becomes:

$$\ddot{y} = \ddot{C}(t)\left[1 - \cos\left(\frac{\pi x}{L}\right)\right], \tag{6.9}$$

and thus the term $\ddot{C}(t) \times 1$ cannot balance with other harmonics. This requires a Galerkin approach instead, however, since the goal is to show a similar trend this was not performed.

The function ODE45 from Matlab was used to solve the above nonlinear ordinary differential equation. The material and model properties were used as same as the experimental specimens. For a simply support beam, the first angular natural frequency is 206 rad/sec. Thus a frequency sweep from 200 rad/sec to 220 rad/sec was applied. Below in Figure 6.10 shows the displacement history of the mid-point of the model under the applied frequency sweep.

In order to switch from time domain to frequency domain, for each time step, the angular frequency value can be calculated using $\omega = a + bt$. In this case, $a = 200$ rad/sec and $b = 0.01$ rad/sec were used for the forward sweep and $a = 220$ rad/sec, $b = -0.01$ rad/sec were used for the backward sweep. The displacement amplitude for each frequency value was determined by taking the maximum value from the displacement response history among the adjacent 50 data points since a very small time step value was used. This method does not provide accurate displacement amplitudes for all frequency values however it is enough to indicate the nonlinear resonance phenomenon. As is illustrated in Figure 6.11, the amplitude-frequency curves show a clear stiffening behavior, which is similar to the experimental results as is shown in Figure 6.5.

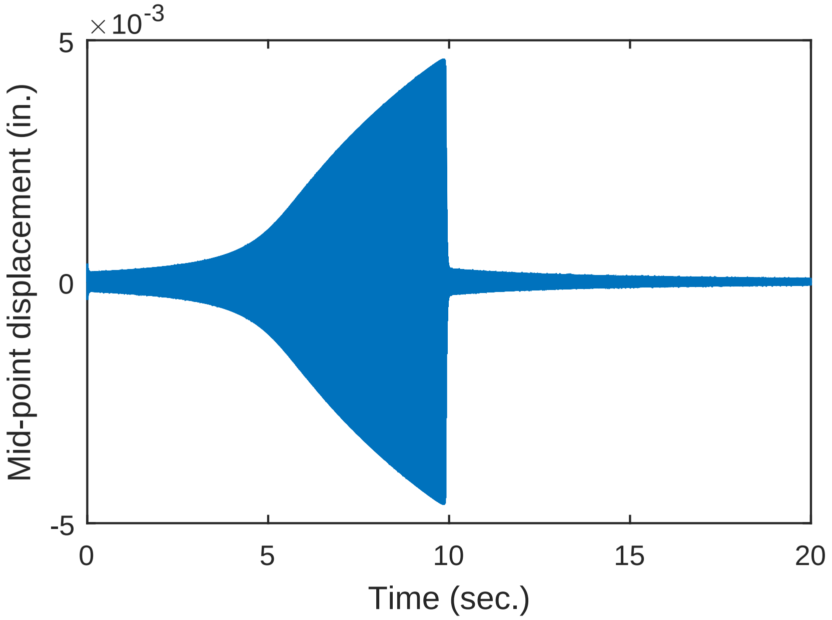

Figure 6.10: Nonlinear resonance displacement history for the mid-point of the model

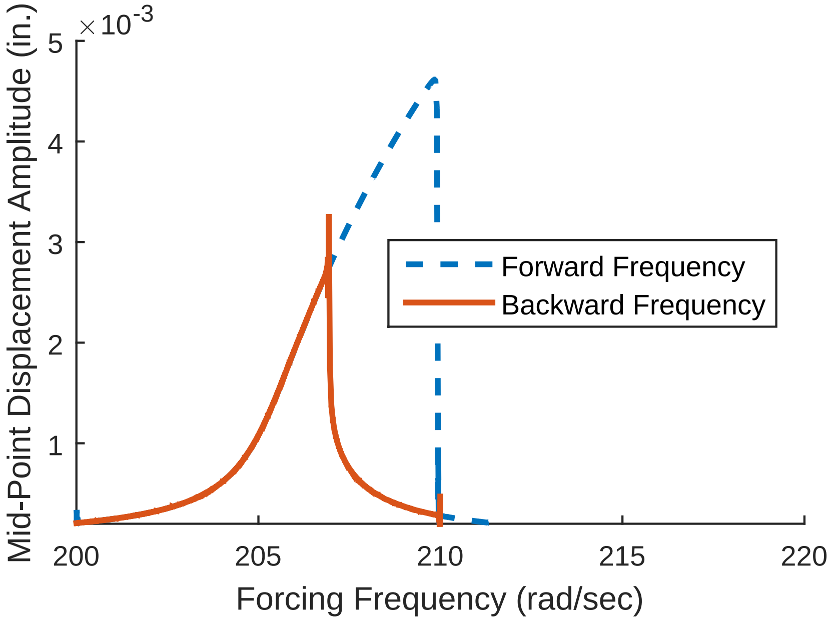

Figure 6.11: Nonlinear resonance from analytical model

6.4 Remarks and Conclusion

In this chapter, large amplitude beam vibration is studied. The stiffness hardening resonance, which is caused by geometric nonlinearity, was investigated both experimentally and analytically for a beam with simplified fixed-fixed boundary conditions. It is substantial to understand the behavior of beam or beam-like elements under large amplitude loading condition for the reason that, as indicated in Figure 6.5, a nonlinear resonance may occur even when forcing frequency does not equal to the natural frequency depending on the force amplitude and initial conditions. An undesired, and highly unexpected (for those familiar with linear vibrations), amplitude jump may occur as it shown in Figure 6.7 due to ambient impact.

Chapter 7

SUMMARY AND FUTURE WORK

7.1 Summary

A beam is one of the most fundamental elements in engineering fields. In this thesis the relationship between the natural frequency and the axial force is studied.

In Chapter 2, the linear relationship between the first squared natural frequency and the axial force within linear elastic region was discovered using analytical closed form solution, numerical model, and experiments. Then in Chapters 3 and 4, the relationship between the two parameters under buckling configuration and tensile plastic deformation were discussed, respectively. It was found that the natural frequencies of a beam reached to zero when it was under the buckling load. Then the squared first natural frequency and the axial force maintained a linear relationship after buckling load. However, the slope change from the linear region to the post-buckling region solved by the theoretical analysis and the numerical model do not exactly agree to each other. Another interesting result is the natural frequency jump in the post-buckling region for a perfect pin-pin or fixed-fixed beam. When the beam is under tensile plastic deformation, it was found experimentally that the linear relationship between the two is no longer true. The squared first natural frequency value softened after reaching the yield load. However, this softening behavior is entirely caused by the length change of the beam. On the contrary, the stiffness was found stiffened within strain hardening region. A bizarre drop of the stiffness from the yielding point to the first data point of the specimens under strain hardening region was also observed.

To further study the effect of the plastic deformation on beam vibration behavior, in Chapter 5 the effect of the plastic deformation on Young's modulus of steel was investigated experimentally. It was found that the Young's modulus of steel dropped when the beam has experienced plastic deformation. However, there is no clear relationship between the amount of percentage drop of Young's modulus and the extent of the plastic deformation. Nevertheless, this phenomenon is really important for its application in whether damage detection or design principle of steel structures.

Finally, large amplitude beam vibration was investigated both experimentally and numerically.

7.2 Future work

In this thesis, the relationship between the first natural frequency and the axial force of buckled beams was studied both theoretically and numerically. Despite the fact that both methods show a linear relationship between the two in post-buckling region, the slopes obtained by the two methods do not agree with each other. Future experimental work is needed to validate the accuracy of the previous theoretical work.

As for beam vibration under tensile plastic deformation, more experiments are needed to validate the drop of the stiffness at the yield point for hot-rolled steel beams. It is also worthwhile to perform the same test on cold-rolled steel in order to validate whether the drop of the stiffness is caused by the plateau from the stress-strain relationship or not. Unfortunately, the numerical dynamic distributed plasticity model developed in this work does not provide good comparison. Future work is needed to better implement the boundary conditions to the model. Axial force effect should also be added to the model based on the algorithm provided in Section 4.4.

REFERENCES

Ansari, M. F. F. S., Mohammadi, V., and Rouhi, H. (2014). "Nonlinear forced vibration analysis of postbuckled beams." *Archive of Applied Mechanics*, 84(3), 421–440.

ASTM (2015). *Standard Test MMethod for Tension Testing of Metallic Materials.* U.S. Department of Defense, ASTM International, 100 Barr Harbor Drive, West Conshohocken, PA 19428-2959, United States, 15a edition.

Bokaian, A. (1988). "Natural frequencies of beams under compressive axial loads." *Journal of Sound and Vibration*, 126(1), 49–65.

Bokaian, A. (1990). "Natural frequencies of beams under tensile axial loads." *Journal of Sound and Vibration*, 142(3), 481–498.

Chopra, A. K. (2012). *Dynamics of Structures: Theory and Applications to Earthquake Engineering, Fourth Edition.* Pearson.

Crisfield, M. (1981). "A fast incremental/iterative solution procedure that handles snap-through." *Computers & Structures*, 13(1-3), 55–62.

Das, D., Sahoo, P., and Saha, K. (2011). "A numerical analysis of large amplitude beam vibration under different boundary conditions and excitation patterns." *Journal of Vibration and Control*, 18(12), 1900–1915.

Eisley, J. (1964). "Large amplitude vibration of buckled beams and rectangular plates." *AIAA Journal*, 2(12), 2207–2209.

Kantz, H. and Schreiber, T. (1997). *Nonlinear Time Series Analysis.* Cambridge University Press.

Khiem, N. T. and Toan, L. K. (2014). "A novel method for crack detection in beam-like structures by measurement of natural frequencies." *Journal of Sound and Vibration*, 333(18), 4084–4103.

Kim, J. T. (2003). "Crack detection in beam-type structures using frequency data." *Journal of Sound and Vibration*, 259(1), 145–160.

Lepidi, M., Gattulli, V., and Vestroni, F. (2009). "Damage identification in elastic suspended cables through frequency measurement." *Journal of Vibration and Control*, 15(6), 867–896.

Malatkar, P. (2003). "Nonlinear vibration of cantilever beams and plates." Ph.D. thesis, Virginia Polytechnic Institute and State University, United States.

Mallow, J. and Lucas, R. (1992). "Multiple resonance in the double-flash effect." *Optical Society of America*, 9(12), 1992.

Mazza, F. and Mazza, M. (2010). "Nonlinear analysis of spatial framed structures by a lumped plasticity model based on the haar-karman principle." *Computational Mechanics*, 45(6), 647–664.

Mazzoni, S. (2012). *Steel Material Modes*. University of California Berkeley, <http://www.ce.berkeley.edu/ filippou/Research/Fedeas/steel.pdf> (Aug 25).

Miller, L. A. (2005). "Structural dynamics and resonance in plants with nonlinear stiffness." *Journal of Theoretical Biology*, 234(4), 511–524.

Newmark, N. (1959). "A method of computation for structural dynamics." *Journal of the Engineering Mechanics Division*, 85(3), 67–94.

Ngo-Huu, C., Kim, S.-E., and Oh, J.-R. (2007). "Nonlinear analysis of space steel frames using fiber plastic hinge concept." *Engineering Structures*, 29(4), 649–657.

Roca, A., Villuendas, A., Mejia, I., Benito, J. A., Llorca-Isern, N., Lluma, J., and Jorba, J. (2014). "Can young's modulus of metallic alloys change with plastic deformation?." *Materials Science Forum*, 783-786, 2382–2387.

Timoshenko, S. (1921). "On the correction for shear of the differential equation for transverse vibration of prismatic bars." *Philosophical Magazine and Journal of Science*, 41(245), 744–746.

van Ballegooijen, M. (2010). "Vibration mitigation using buckled beams." M.S. thesis, Eindhoven University of Technology, The Netherlands.

Virgin, L. N. (1993). "Effect of axial load on forced vibration of beams." *Journal of Sound and Vibration*, 168(3), 395–405.

Virgin, L. N. (2007). *Vibration of Axially Loaded Structures.* Cambridge University Press, England, 2nd edition.

Wiebe, R. (2012). "Nonlinear dynamics of discrete and continuous mechanical systems with sanp-through instabilities." Ph.D. thesis, Duke University, United States.

Wiebe, R. and Virgin, L. N. (2016). "On the experimental identification of unstable static equilibria." *Proceedings of the Royal Society of London A: Mathematical, Physical and Engineering Sciences*, 472(2190), 20160172.

Yuen, M. M. F. (1985). "A numerical study of the eigenparameters of a damaged cantilever." *Journal of Sound and Vibration*, 103(3), 301–310.